

SIMPonium bound states of complex scalar dark matter: Relic density and astrophysical signatures

Pa. Gokhula Prasad,^a V. Suryanarayana Mummidi^a

^a*Department of Physics, National Institute of Technology, Tiruchirappalli, India*

E-mail: pa.gokhul1998@gmail.com, venkata@nitt.edu

ABSTRACT: We study a strongly interacting complex scalar dark matter candidate (χ), subject to an attractive potential mediated by a vector boson A^μ . Such interactions allow χ to form bound states: SIMPonium. In this work, we systematically investigate the bound state dynamics of our dark sector, including the formation and decay of SIMPonium and its influence on the thermal history. Our analysis shows in absence of any bound state formation χ freezes out at $x \approx 16$ and the presence of SIMPonium in the thermal bath slightly modifies the freeze out behaviour of the free χ particles, which freezes out at $x \approx 20$. While the bound state itself remains in chemical equilibrium for a longer duration and freezes out at a significantly later time, $x \approx 250$. We compute the indirect energy spectra arising from free dark matter annihilation and SIMPonium decay, where the resulting Standard Model particles subsequently produce both final state radiation and radiative decay spectra. We find that the total differential photon flux from dark matter with mass $m_\chi = 150$ MeV lies in the range $E_\gamma^2 \frac{d\phi}{d\Omega dE_\gamma} \in [10^{-27}, 10^{-17}] \text{ MeV cm}^{-2} \text{ s}^{-1} \text{ sr}^{-1}$, for photon energies in the interval $E_\gamma \in [10^{-3}, 10^2]$ MeV. The predicted signal is therefore exceedingly feeble and remains well below the sensitivity of current experimental facilities.

Contents

1	Introduction	1
2	Model	3
3	Abundance of SIMPonium and free χ	4
4	Bound state dynamics	7
4.1	SIMPonium formation	8
4.2	De-excitation of SIMPonium	9
4.3	Stability of SIMPonium	11
4.4	Annihilation of free χ	13
5	Indirect detection	14
5.1	Final-state radiation	15
5.2	Radiative decay	17
5.3	Full spectrum	19
6	Conclusion	20
A	Coulomb wavefunctions	21
A.1	Bound state wavefunction	21
A.2	Scattering state wavefunction	22
B	Perturbative matrix elements	22
B.1	Matrix elements for σ_{BSF} and Γ_{Trans}	22
B.2	Matrix elements for Γ_{B_n} and σ_{Ann}	24
C	Calculation of thermal average cross sections	25
C.1	$4\chi \rightarrow 2\chi$ annihilation cross sections	25
C.2	Bound state dynamics cross sections	27

1 Introduction

The Planck satellite determined the dark matter abundance to be $\Omega h_{DM}^2 = 0.12$, indicating that dark matter constitutes nearly 25% of the present Universe [1]. The leading cold dark matter candidate known as Weakly Interacting Massive Particles (WIMP), naturally reproduces this relic abundance through the WIMP miracle [2]. This theoretical appeal motivated extensive direct [3–5], collider [6–8] and indirect searches [9–14]. Despite decades of effort, no conclusive evidence for WIMP dark matter has been obtained [15–18]. The

absence of experimental confirmation strongly motivates the consideration of alternative dark matter scenarios.

This need for alternatives becomes even more pressing when viewed alongside the well known small scale challenges of the Λ CDM model, such as core cusp and too big to fail problems [19, 20]. A particularly compelling alternative is self-interacting dark matter (SIDM) which would solve the small scale issues [21, 22]. If these self-interactions are sufficiently strong while the coupling to the Standard Model remains extremely weak, the framework naturally extends to the Strongly Interacting Massive Particle (SIMP) paradigm [23, 24]. In this scenario, the observed relic abundance is achieved through the “SIMP miracle,” where number changing $4 \rightarrow 2$ interactions in the dark sector govern thermal freeze out of dark matter [25, 26].

In this work, we consider a complex scalar field χ as the dark matter candidate, stabilized by both a Z_2 symmetry and a dark $U(1)$ gauge symmetry. The dark matter particles interact through an attractive Coulomb potential mediated by a massless dark photon A^μ . These interactions permit the formation of dark bound states by emitting a mediator, which we refer to as SIMPonium (B_n). Similar studies such as bound state formation formed by WIMP dark matter and non radiative SIMP bound state formation and its impact on relic density has been studied [27–30]. In this work we analyze the impact due to radiative bound state formation by using the formalism suggested by [29]. We also examine the possibility that bound states may form not only in the ground state but also in higher excited states, and we specifically study the ground state and the first two excited levels of SIMPonium ($B_{n'}$). We demonstrate that even in the presence B_n and $B_{n'}$, our model is capable of reproducing the observed dark matter relic abundance. The formation of bound states slightly reduces the free dark matter yield compared to the scenario without bound state effects and the abundance of bound states are very less compared to abundance of free dark matter.

We investigate the processes by which these bound states are formed through mediator emission, as well as how the excited SIMPonium states transition to lower states by radiating a dark photon. Furthermore, we analyze the stability of these bound states by examining their decay into dark radiation and ionization rates of bound states. In addition, we explore the possibility in which dark matter particles annihilate into Standard Model states instead of forming bound states. Although SIMPonium can decay into massless dark photons, the mediator mass $m_A = 0$ prevents these dark photons from communicating with Standard Model particles, even in the presence of a kinetic mixing portal [31]. This drastically suppresses the possibility of generating visible signals through dark radiation. Therefore, in this work we employ the Higgs portal as the primary channel connecting the dark sector to the visible sector. All of these processes are studied across three astrophysical environments:- galaxy clusters, the galactic center, and dwarf galaxies, each characterized by different relative velocities v_{rel} of the incoming particles.

Even though the signals arising purely from dark radiation are invisible, our dark matter candidate can still produce observable signatures through two key mechanisms: (i) annihilation of free χ particles into Standard Model states, and (ii) the decay of SIMPonium bound states into Standard Model particles. We compute the resulting spectra from

final-state radiation [32] as well as from radiative decays of the Standard Model particles produced in these processes [33].

To analyze these signals in each astrophysical environment, we incorporate the appropriate J -factors for free dark matter annihilation and the corresponding D -factors for SIMPonium decay, allowing us to systematically study the indirect detection prospects of this model.

The paper is structured as follows. In Section 2, we introduce the complex scalar χ as dark matter candidate, derive the interaction potential between two dark matter particles, and obtain the corresponding wavefunctions of the resulting potential. In Section 3, we solve the coupled Boltzmann equations governing the evolution of the abundances of both free and bound dark matter, demonstrating how the model reproduces the observed relic density. Section 4 focuses on the dynamics of the bound states, including bound-state formation, decay, ionization, de-excitation of excited states, and the annihilation of free dark matter. In Section 5, we explore the indirect detection prospects of the model by computing the photon spectra arising from final-state radiation and radiative decays. Finally, Section 6 summarizes our study and presents our main conclusions.

2 Model

Bound state formation within the SIMP paradigm requires a dark sector capable of both strong self interactions and efficient number changing process. To capture these features in a minimal model, we consider a complex scalar dark matter candidate χ interacting through the Lagrangian,

$$\mathcal{L} = g_\chi \chi^* A^\mu \chi + \frac{\lambda_\chi}{4!} |\chi|^4.$$

The gauge coupling g_χ provides the attractive force necessary for SIMPonium formation [34], while the quartic term proportional to λ_χ enables the $4\chi \rightarrow 2\chi$ annihilation responsible for obtaining the correct relic density [24, 26]. For the rest of the discussion, we consider the following toy model incorporating these interactions.

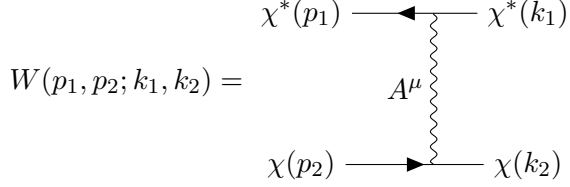
We choose a minimal model where χ is a complex scalar and the attraction between them is mediated by a vector boson A^μ . The dark matter candidate is stabilized by an unbroken Z_2 and a dark $U(1)$ symmetry:

$$\mathcal{L} = -\frac{1}{4} F_\chi^{\mu\nu} F_{\chi\mu\nu} + |D_\mu \chi|^2 - m_\chi^2 |\chi|^2 - \frac{\lambda_\chi}{4!} |\chi|^4 - \frac{\lambda_{\chi H}}{4!} |\chi|^2 H^\dagger H, \quad (2.1)$$

where $D_\mu = \partial_\mu + ig_\chi A^\mu$, and g_χ is the interaction strength between the mediator and dark matter. The dark photon remains massless and cannot communicate with the Standard Model, even if a kinetic mixing term is included [35].

At lowest order, the attractive force between χ^* and χ arises from the exchange of the

vector boson A^μ , represented by the diagram:



In the non-relativistic limit, the scattering amplitude simplifies to,

$$W(p_1 - k_1) = \frac{4m_\chi^2 g_\chi^2}{(p_1 - k_1)^2}.$$

The corresponding interaction potential is given by [36],

$$V(r) = \frac{i}{4\mu m_\chi} \int \frac{d^3 p}{(2\pi)^3} W(p) e^{-ip \cdot r},$$

which results in an attractive Coulomb potential,

$$V(r) = -\frac{V_0}{r}, \quad V_0 > 0,$$

where $V_0 = \frac{g_\chi^2}{4\pi}$ is the interaction strength and $\mu = \frac{m_\chi}{2}$ is the reduced mass.

The Coulomb potential gives two classes of eigen states: discrete bound levels and a continuous energy spectrum. The continuous spectrum corresponds to scattering states of free dark matter particles and is characterized by a continuous quantum number associated with the expectation value of the relative momentum, $k = \mu v_{\text{rel}}$. In contrast, the discrete spectrum represents the bound states of dark matter, defined by discrete nlm quantum numbers. We extend the analysis up to $n = 3$ to examine the properties of the corresponding excited states.

The bound state $\Psi(r)_n$ and scattering state $\Psi(r)_s$ of SIMPonium under this potential are [37],

$$\Psi(r)_n = N_{nlm} r^l e^{-\sqrt{\alpha}r} L_n^{2l+1}(2r\sqrt{\alpha}) Y_m^l(\theta, \phi), \quad (2.2)$$

$$\Psi(r)_s = N e^{ik \cdot r} {}_1F_1(-i\delta; 1; i(kr - k \cdot r)). \quad (2.3)$$

Here, $L_n^{2l+1}(2r\sqrt{\alpha})$ is the associated Laguerre polynomial, and ${}_1F_1(-i\delta; 1; i(kr - k \cdot r))$ is the confluent hypergeometric function of the first kind. A detailed derivation is presented in Appendix A.

3 Abundance of SIMPonium and free χ

Many dark matter models such as WIMPs, maintains thermal equilibrium with the Standard Model bath in the early Universe through annihilation processes of the form $\chi\chi^* \rightarrow \text{SM} \bar{\text{SM}}$ [38, 39]. Unlike WIMPs, SIMP dark matter particles follow the inequality relation [25],

$$\Gamma_{\chi+\text{SM} \rightarrow \chi+\text{SM}} \gtrsim \Gamma_{4\chi \rightarrow 2\chi} \gg \Gamma_{2\chi \rightarrow 2\text{SM}}, \quad (3.1)$$

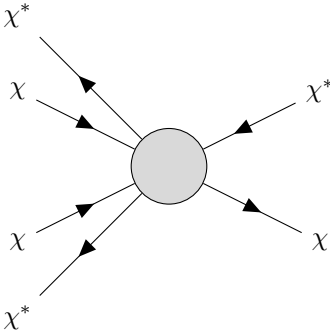


Figure 1: Feynman diagram illustrating the $4\chi \rightarrow 2\chi$ number changing process.

Label	Process
A	$\chi + \chi^* \rightarrow B_n + A^\mu$
B	$B_n + A^\mu \rightarrow \chi + \chi^*$
C	$\chi + \chi + \chi^* + \chi^* \rightarrow \chi^* + \chi$
D	$\chi + \chi + \chi^* + \chi^* \rightarrow B_n + A^\mu$
E	$\chi + \chi^* + B_n \rightarrow \chi + \chi^*$
F	$B_n + B_n \rightarrow \chi + \chi^*$
G	$\chi + \chi^* + B_n \rightarrow B_n + A^\mu$
H	$B_n + B_n \rightarrow B_n + A^\mu$
I	$B_n \rightarrow A^\mu + A^\mu$
J	$B_{n'} + A^\mu \rightarrow B_n + A^\mu$

Table 1: List of relevant SIMP and bound state processes for relic abundance.

where $\Gamma_{\chi+\text{SM} \rightarrow \chi+\text{SM}} = n_\chi^{eq} \langle \sigma v \rangle$, $\Gamma_{4\chi \rightarrow 2\chi} = n_\chi^3 \langle \sigma v^3 \rangle$ and $\Gamma_{2\chi \rightarrow 2\text{SM}} = n_\chi \langle \sigma v \rangle$. The condition imposed by Eq. (3.1) suggests that the interaction rate for dark matter annihilation into standard model particles ($\chi\chi^* \rightarrow \text{SM}\bar{\text{SM}}$) is feeble and number density of χ changes primarily due to self interactions such as $4\chi \rightarrow 2\chi$. Despite the feeble coupling between the dark and visible sectors, the large number density of Standard Model particles enhances the $\chi\text{SM} \rightarrow \chi\text{SM}$ scattering rate sufficient enough to maintain thermal equilibrium between the two sectors.

In scenarios where bound states do not form, the thermal evolution of χ would be determined by a simplest $4\chi \rightarrow 2\chi$ interaction, $\chi\chi\chi^*\chi^* \rightarrow \chi^*\chi$. On the flip side, the scenarios in which bound states could form, new particles such as SIMPonium ground state B_n and its excited state $B_{n'}$ would coexist along with free dark matter χ . The presence B_n and $B_{n'}$ would modify the evolution of dark matter abundance by introducing new $4\chi \rightarrow 2\chi$ annihilation process involving bound states. All such processes relevant for the Boltzmann evolution are listed in Table 1 and the following discussion highlights key features of these interactions. Following bound state formation through channels A and D, the bound states undergo further evolution via the processes labeled B, E, F, G, H, I, and J. Among these, only process G preserves the bound state number density. In contrast, processes B, E,

F, I, and J modify the bound state number density, where B, I, and J corresponds to SIMPonium ionization, decay and de-excitation, respectively.

The thermal evolution of the dark matter particle χ and the bound state B_n is governed by a set of coupled Boltzmann equations written in terms of the yield variables $Y_\chi = \frac{n_\chi}{s}$ and $Y_B = \frac{n_B}{s}$, where n_χ and n_B denote the number densities of the free dark matter particles and the bound states, respectively, and s is the entropy density of the Universe. It is convenient to parametrize the evolution using the dimensionless variable $x = \frac{m_\chi}{T}$, where m_χ is the dark matter mass and T denotes the temperature of the standard model thermal bath. The Boltzmann equations describing the evolution of the dark matter and SIMPonium abundances are given in Eq. (3.2) and (3.3). The right-hand sides of these equations contain the relevant number changing collision terms, involving $\langle \sigma v \rangle$, $\langle \sigma v^2 \rangle$, $\langle \sigma v^3 \rangle$ and the analytical expressions for these cross sections are derived in detail in Appendix C.

$$\frac{dY_\chi}{dx} = \frac{x}{sH(m)} \left[-s^2 \langle \sigma v \rangle_A \left(Y_\chi^2 - \frac{(Y_\chi^{\text{eq}})^2 Y_{B_n} Y_{A^\mu}}{Y_{B_n}^{\text{eq}} Y_{A^\mu}^{\text{eq}}} \right) + s^2 \langle \sigma v \rangle_B \left(Y_{A^\mu} Y_{B_n} - \frac{Y_\chi^2 Y_{B_n}^{\text{eq}} Y_{A^\mu}^{\text{eq}}}{(Y_\chi^{\text{eq}})^2} \right) \right. \\ - s^4 \langle \sigma v^3 \rangle_C \left(Y_\chi^4 - (Y_\chi^{\text{eq}})^2 Y_\chi^2 \right) - s^4 \langle \sigma v^3 \rangle_D \left(Y_\chi^4 - \frac{(Y_\chi^{\text{eq}})^4 Y_{B_n} Y_{A^\mu}}{Y_{B_n}^{\text{eq}} Y_{A^\mu}^{\text{eq}}} \right) \\ \left. + s^2 \langle \sigma v \rangle_F \left(Y_{B_n}^2 - \frac{(Y_{B_n}^{\text{eq}})^2 Y_\chi^2}{(Y_\chi^{\text{eq}})^2} \right) - s^3 \langle \sigma v^2 \rangle_G \left(Y_{B_n} Y_\chi^2 - \frac{(Y_\chi^{\text{eq}})^2 Y_{B_n} Y_{A^\mu}}{Y_{A^\mu}^{\text{eq}}} \right) \right], \quad (3.2)$$

$$\frac{dY_{B_n}}{dx} = \frac{x}{sH(m)} \left[s^2 \langle \sigma v \rangle_A \left(Y_\chi^2 - \frac{(Y_\chi^{\text{eq}})^2 Y_{B_n} Y_{A^\mu}}{Y_{B_n}^{\text{eq}} Y_{A^\mu}^{\text{eq}}} \right) - s^2 \langle \sigma v \rangle_B \left(Y_{A^\mu} Y_{B_n} - \frac{Y_\chi^2 Y_{B_n}^{\text{eq}} Y_{A^\mu}^{\text{eq}}}{(Y_\chi^{\text{eq}})^2} \right) \right. \\ + s^4 \langle \sigma v^3 \rangle_D \left(Y_\chi^4 - \frac{(Y_\chi^{\text{eq}})^4 Y_{B_n} Y_{A^\mu}}{Y_{B_n}^{\text{eq}} Y_{A^\mu}^{\text{eq}}} \right) - s^3 \langle \sigma v^2 \rangle_E \left(Y_\chi^2 Y_{B_n} - (Y_\chi^{\text{eq}})^2 Y_{B_n}^{\text{eq}} \right) \\ - s^2 \langle \sigma v \rangle_F \left(Y_{B_n}^2 - \frac{(Y_{B_n}^{\text{eq}})^2 Y_\chi^2}{(Y_\chi^{\text{eq}})^2} \right) - s^2 \langle \sigma v \rangle_H \left(Y_{B_n}^2 - \frac{Y_{B_n}^{\text{eq}} Y_{B_n} Y_{A^\mu}}{Y_{A^\mu}^{\text{eq}}} \right) \\ \left. - s \langle \Gamma_I \rangle \left(Y_{B_n} - \frac{Y_{B_n}^{\text{eq}} (Y_{A^\mu})^2}{(Y_{A^\mu}^{\text{eq}})^2} \right) + s \langle \Gamma_J \rangle \left(Y_{B_n} - \frac{Y_{B_n}^{\text{eq}} Y_{B_n} Y_{A^\mu}}{Y_{A^\mu}^{\text{eq}} Y_{B_n}^{\text{eq}}} \right) \right]. \quad (3.3)$$

We also study the evolution of χ in the absence of bound-state formation by solving the corresponding Boltzmann equation:

$$\frac{dY_{\text{free}}}{dx} = \frac{-x}{H(m)} s^3 \langle \sigma v^3 \rangle_C \left(Y_\chi^4 - (Y_\chi^{\text{eq}})^2 Y_\chi^2 \right). \quad (3.4)$$

In Fig. 2, we present the numerical solutions of Y_χ , Y_B and Y_{free} obtained by solving Eq. (3.2), (3.3) and (3.4). In the absence of bound states, the evolution of dark matter is solely governed by $\langle \sigma v^3 \rangle_C$, and Y_χ follows its equilibrium value, $Y_\chi = Y_\chi^{\text{eq}}$, until chemical decoupling occurs at $x_1 \approx 16$. However, in the presence of bound states, process D becomes kinematically allowed and since it is slightly stronger than process C, it governs

$$m_\chi = 150 \text{ MeV}, g_\chi = 0.7, \lambda_\chi = 0.8$$

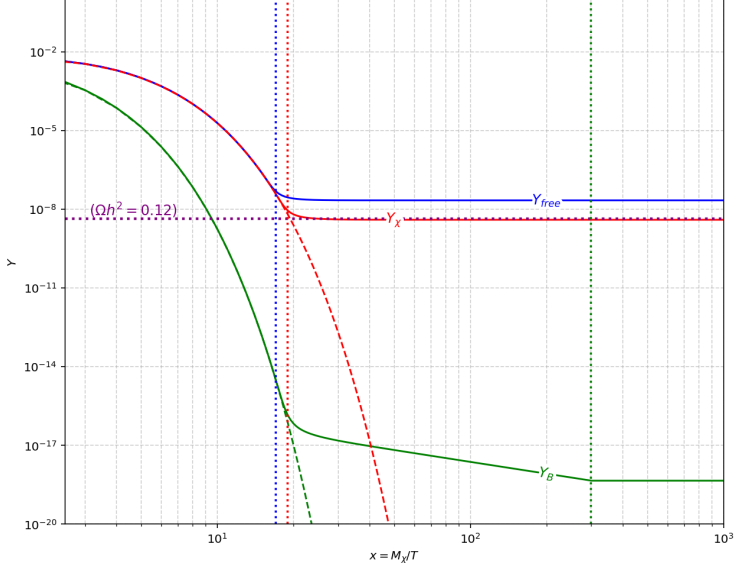


Figure 2: Evolution of the number densities of free dark matter (Y_χ), SIMPonium (Y_B), and dark matter abundance in the absence of bound state formation (Y_{free}). The observed relic density $\Omega h^2 = 0.12 \pm 0.0012$ is indicated by the purple dotted line.

the evolution of free χ until freeze out at $x_2 \approx 20$. For $x > x_2$, the dark sector is not completely decoupled despite the freeze out of free χ , because the processes $\langle \sigma v \rangle_F$, $\langle \sigma v^2 \rangle_E$, $\langle \sigma v^2 \rangle_G$, $\langle \sigma v \rangle_H$, $\langle \Gamma_I \rangle$ and $\langle \Gamma_J \rangle$ are still relevant in this epoch and these would determine the abundance of B_n . While in the case of non radiative bound state formation the depletion of the SIMPonium abundance continues only until $x \approx 110$ [30], for radiative bound-state formation we find a substantially longer depletion period, which occurs at $x_B \approx 250$.

In this study, we found all cross section scale as $\langle \sigma v \rangle \approx x^\gamma$ where $\gamma < 1$, therefore even in the presence of excited states we obtain the correct relic density [40] and the total relic density of dark matter is then obtained as [41],

$$\begin{aligned} \Omega h^2 &= 2.752 \times 10^5 (\Omega_\chi h^2 + \Omega_B h^2) \\ &= 2.752 \times 10^5 \left[\left(\frac{m_\chi}{\text{MeV}} \right) Y_\chi(x \rightarrow \infty) + \left(\frac{m_B}{\text{MeV}} \right) Y_B(x \rightarrow \infty) \right]. \end{aligned} \quad (3.5)$$

Since the bound states evolve for a much longer duration than χ , their final yield becomes negligible compared to that of χ . Consequently, Eq. (3.5) can be approximated as,

$$\begin{aligned} \Omega h^2 &\approx 2.752 \times 10^5 (\Omega_\chi h^2) \\ &\approx 2.752 \times 10^5 \left[\left(\frac{m_\chi}{\text{MeV}} \right) Y_\chi(x \rightarrow \infty) \right]. \end{aligned} \quad (3.6)$$

4 Bound state dynamics

Following the freeze out of bound states and free χ , residual interactions may still occur at the current epoch. While these interactions offer potential observational signatures, their

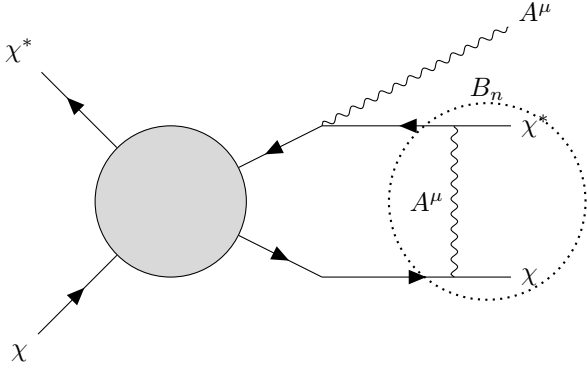


Figure 3: Feynman diagram for bound state formation via emission of a vector boson in the process $\chi^* \chi \rightarrow B_n A^\mu$.

impact on the total relic density remains negligible [41]. In this section, we classify astrophysical environments according to the relative velocity of incoming particles as galactic center, dwarf galaxies, galaxy clusters [42–45] and investigate potential observation signals produced by residual interactions of free χ and SIMPonium. In particular, we examine bound state formation, radiative de excitation of excited states, ionization processes, decay of bound state and dark matter annihilations within these environments. This analysis is performed over the parameter region consistent with the observed relic abundance, with the dark matter mass in the range $0 < m_\chi \leq 1000$ MeV, coupling $g_\chi \in [0.48, 0.88]$, quartic coupling $\lambda_\chi \in [0.5, 0.7]$ and dark matter higgs coupling $\lambda_{\chi H} = 10^{-3}$.

4.1 SIMPonium formation

When two dark matter particles approach each other, they can radiatively lose energy by emitting a massless mediator A^μ and form a bound state. The corresponding bound state formation process is illustrated in Fig. 3, while the relevant matrix element and cross section are given in Eq. (4.1) and (4.2), respectively [46],

$$\mathcal{M}_n = \sqrt{\frac{2}{\mu}} \int \frac{d^3 p}{(2\pi)^3} \frac{d^3 q}{(2\pi)^3} \psi_n^*(p) \psi_s(q) M^{\text{Pert}}(p, q), \quad (4.1)$$

$$\sigma_{\text{BSF}} = \frac{|P_{\text{cm}}| |\mathcal{M}_n|^2}{64\pi m_\chi^2 \mu v_{\text{rel}}}. \quad (4.2)$$

The transition matrix element is governed by the overlap of the initial scattering state ψ_s and the final n^{th} state bound state wavefunctions ψ_n . Here, μ is the reduced mass of the two particle system, and $M^{\text{Pert}}(p, q)$ represents the perturbative amplitude for the process, which is derived in appendix B.1. Furthermore, m_χ denotes the dark matter mass, and $P_{\text{cm}} = \epsilon_k - \epsilon_n$ is the center of mass momentum, where ϵ_k and ϵ_n are the energies of the scattering and bound states, respectively

From Fig. 4(a), it is evident that less massive dark matter particles forms bound state more effectively. This behavior is a expected as the cross section scales $\sigma_{\text{BSF}} \propto 1/m_\chi^2$ and the binding energy for a Coulomb potential is less for low μ [37]. Furthermore, because the

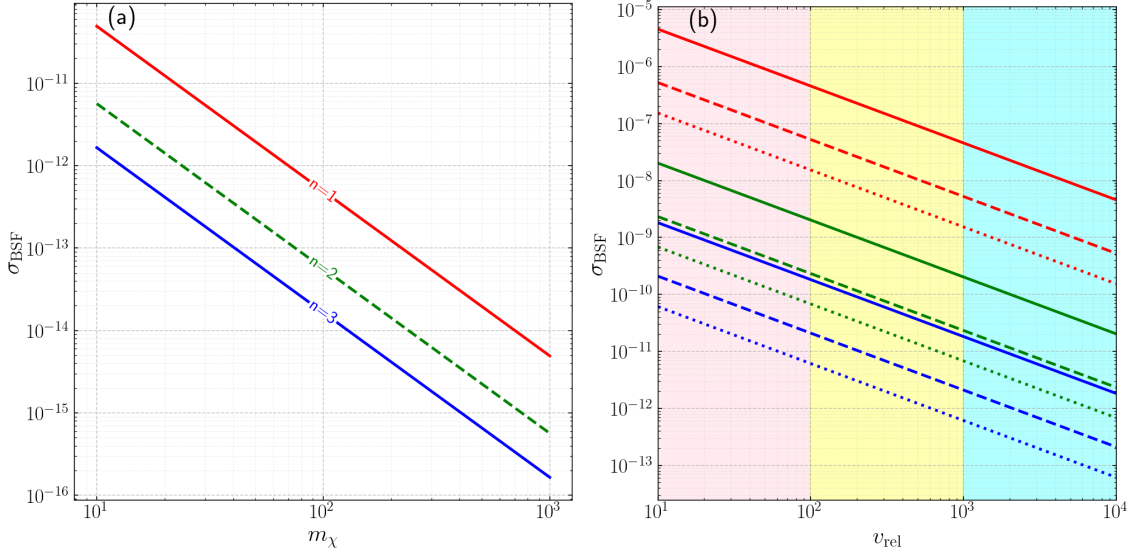


Figure 4: Panel (a) shows the SIMPonium formation cross section (for $v_{\text{rel}} = 3000$ km/s) as a function of the dark matter mass, varied from 0 to 1000 MeV, for the ground state and the first and second excited states. Panel (b) illustrates the dependence of the cross section on the relative velocity v_{rel} in km/s, where the red, green, and blue curves correspond to $m_\chi = 10$ MeV, 150 MeV, and 500 MeV, respectively. Solid, dashed, and dotted lines represent the $n = 1$, $n = 2$, and $n = 3$ states, respectively. The red-shaded region represents dwarf galaxies, the yellow corresponds to the galactic center, and the blue indicates galactic clusters.

bound state wavefunction scales as $|\psi_n(r)|^2 \propto n^{-3}$, the production of excited SIMPonium states is suppressed.

The velocity dependence of σ_{BSF} is shown in Fig. 4(b), with shaded regions corresponding to v_{rel} of dark matter at dwarf galaxies (red), the galactic center (yellow), and galaxy clusters (blue). Since cross section scales as $\sigma_{\text{BSF}} \propto 1/v_{\text{rel}}$, even in the presence of a strong attractive force, the interaction is not sufficient to efficiently form bound states in high-velocity regions such as galactic clusters and bound states are more likely to form in low v_{rel} regions such as dwarf galaxies and the galactic center.

4.2 De-excitation of SIMPonium

If the bound state is initially produced in an excited level, it does not remain there permanently. Instead, it can undergo a radiative transition to a lower energy state by emitting a dark photon. This de-excitation process is analogous to atomic transitions in ordinary matter and can occur through a series of steps until the SIMPonium reaches the ground state. The corresponding process is depicted in Fig. 5, while the relevant matrix element and de-excitation rate are given in Eq. (4.3) and (4.4),

$$\mathcal{M}_n = \int \frac{d^3 p}{(2\pi)^3} \frac{d^3 q}{(2\pi)^3} \psi_n(p) \psi'_n(q) M^{\text{Pert}}(p, q), \quad (4.3)$$

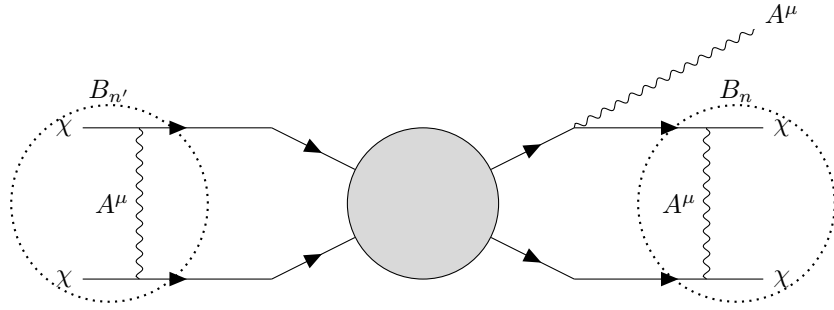


Figure 5: Feynman diagram illustrating the de-excitation of an excited SIMPonium state to the ground state via emission of a vector boson in the process $B_{n'} \rightarrow B_n A^\mu$.

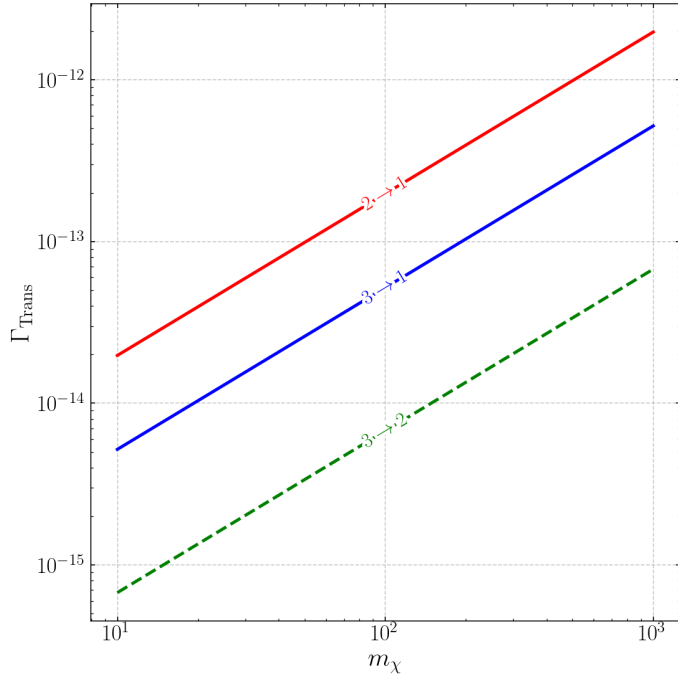


Figure 6: The figure shows the radiative de-excitation cross section of SIMPonium as a function of the dark matter mass, varied from 0 to 1000 MeV, for transitions from excited to lower energy states.

$$\Gamma_{\text{Tran}} = \frac{|P_{\text{cm}}| |\mathcal{M}_n|^2}{16\pi m_\chi^2 \mu}. \quad (4.4)$$

The transition matrix elements are given by overlap of lower SIMPonium states $\psi_n(p)$ and excited SIMPonium states $\psi_{n'}(q)$. In these equations, $M^{\text{Pert}}(p, q)$ represents the perturbative amplitude for the de-excitation process (see appendix B.1) and $P_{\text{cm}} = \epsilon_{n'} - \epsilon_n$ is the center of mass momentum of the emitted dark photon, where $\epsilon_{n'}$ and ϵ_n denote the energies of the excited and lower SIMPonium states.

The dependence of the radiative de-excitation process on the dark matter mass is il-

lustrated in Fig. 6, in contrast to the SIMPonium formation cross section the de-excitation rate scales as $\Gamma_{\text{Trans}} \propto m_\chi$ and radiative de-excitation is independent of the relative velocity v_{rel} . In low velocity environments such as dwarf galaxies where the population of excited states is relatively larger than in other regions, we therefore expect an enhanced emission of dark photons from de-excitation. In contrast, the galactic center and galaxy clusters would show medium and low dark photon fluxes, respectively, due to the smaller abundance of excited bound states. Excited SIMPonium states have a high probability of transitioning directly to the ground state, bypassing the need of metastable intermediate states. Consequently, dark photons with frequencies $\nu \propto E_2 - E_1$ and $\nu \propto E_3 - E_1$ are expected to appear more frequently than those with $\nu \propto E_3 - E_2$ and the presence of these dark photon fluxes in various regions can significantly influence the ionization of bound states as shown in the next section. While we assume a massless mediator for simplicity in this study, if instead the interaction between dark matter particles were mediated by a massive force carrier, the resulting dark photon emitted at different frequencies would provide distinct signatures for experimental searches and indirect detection probes [47, 48].

4.3 Stability of SIMPonium

After the bound state of χ is formed it can be broken in two ways: (a) an energetic dark photon can hit the SIMPonium and dissociate it into its constituents, and (b) the bound state itself can be unstable and decay into dark radiation.

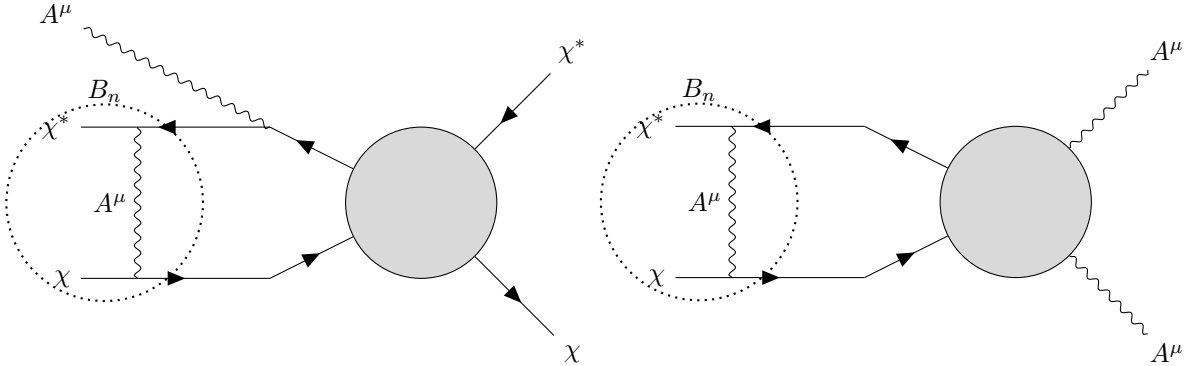


Figure 7: Feynman diagrams showing: (a) Dissociation of SIMPonium by absorption of a dark photon, (b) Decay of the bound state into dark radiation.

The transition amplitude for decay process given in Eq. (4.5) (see appendix B.2) . The cross sections for ionization of SIMPonium would be related by Milne relation [40, 49, 50] as shown in Eq. (4.7) and decay rate would be given by Eq. (4.6),

$$\mathcal{M}_n^{\text{dec}} = \sqrt{\frac{1}{2\mu}} \int \frac{d^3 p}{(2\pi)^3} \psi_n^*(p) M^{\text{Pert}}(p), \quad (4.5)$$

$$\Gamma_{B_n} = \sigma_0 |\psi_n(0)|^2. \quad (4.6)$$

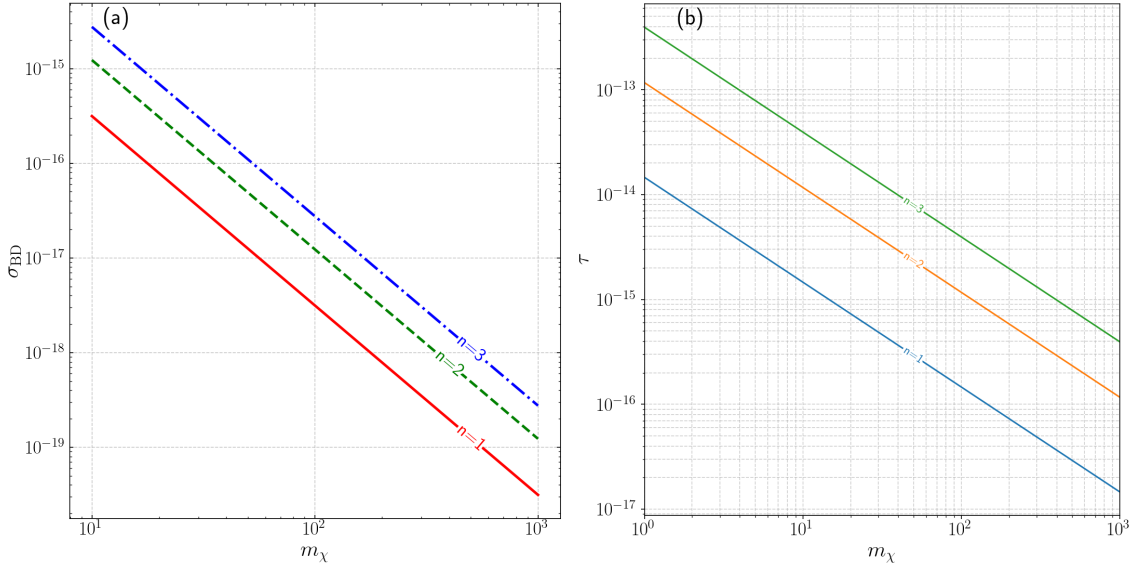


Figure 8: Panel (a) shows the ionization cross section for SIMPonium as a function of the dark matter mass, varied from 0 to 1000 MeV, for $n = 1$, $n = 2$ and $n = 3$ states. Panel (b) shows the lifetime (in seconds) of SIMPonium states as function of m_χ in MeV for all three states.

$$\sigma_{\text{BD}} = \frac{\mu^2 v_{\text{rel}}^2}{2\omega^2} \sigma_{\text{BSF}}, \quad (4.7)$$

where $\psi_n(p)$ is the n^{th} SIMPonium wavefunctions and $\omega = E_n + \frac{\mu v_{\text{rel}}^2}{2}$ is the energy of the incoming photon, σ_0 is perturbative cross section. In this model, the bound state is formed between a particle antiparticle pair, making it possible for the bound state to decay into a pair of mediators A^μ and this decay of the bound state makes SIMPonium unstable as shown in Fig. 8(b). Furthermore, due to their weak coupling with the standard model, their decay into standard model particles is also highly suppressed compared to decay into A^μ . The behavior of ionization cross section for varying dark matter mass is presented in Fig. 8(a). Similar to bound state formation, the ionization cross section of SIMPonium scales as $\sigma_{\text{BD}} \propto m_\chi^{-2}$, and because heavier SIMPonium has a larger binding energy than lighter states, dark photons more efficiently ionize lighter bound states while ionization of heavier ones is suppressed. Given the short lifetime of the bound state, we conclude that SIMPonium is unstable and they have high probability of decaying into dark photons rather than getting ionized into free dark matter.

In galaxy clusters, the formation of SIMPonium bound states is already suppressed, and any excited bound states that do form are efficiently ionized due to their relatively large ionization cross sections, whereas radiative de-excitation further ensures that the remaining SIMPonium are in ground state. In dwarf galaxies and galactic centers, the breakdown occurs more often than expected because of the high flux of dark photons originating from comparatively higher bound state formation. As a result, more massive ground states are

efficiently produced and remain largely unionized. Due to their shorter lifetimes, massive ground state SIMPonium subsequently decay into dark photons, while less massive excited bound states are ionized faster.

4.4 Annihilation of free χ

Two dark matter candidates can annihilate into standard model particles as shown in Fig. 9. To maintain minimality, we adopt a Higgs portal to mediate the interaction between dark matter and the standard model, while the dark photon A^μ remains effectively decoupled in this model.

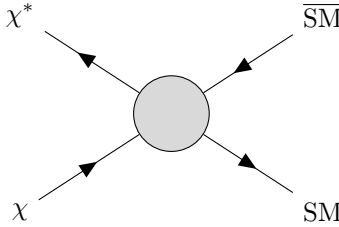


Figure 9: Feynman diagram illustrating the annihilation of free dark matter into a pair of standard model particles in the process $\chi^* \chi \rightarrow S M \overline{S} \overline{M}$.

The transition amplitude for this process and corresponding cross section would be given by Eq. (4.8) (see appendix B.2) and Eq. (4.9),

$$\mathcal{M}_n = \int \frac{d^3 p}{(2\pi)^3} \psi_s(p) M^{\text{Pert}}(p), \quad (4.8)$$

$$\sigma_{\text{Ann}} = \frac{|\mathcal{M}_n|^2 |P_{\text{cm}}|}{64\pi m_\chi^2}, \quad (4.9)$$

where $\psi_s(p)$ is wavefunction of scattering states for coulomb potential and $|P_{\text{cm}}|$ denotes the center of mass momentum.

The variation of the annihilation cross section with respect to m_χ is presented in Fig. 10(a). It is observed that the cross section increases with the dark matter mass. For low mass dark matter, kinematically dark matter can annihilate only into $e^+ e^-$ pairs. However, due to the m_f/v_h scaling of the Higgs portal coupling, this channel is strongly suppressed relative to heavier leptonic or hadronic final states [25].

For larger dark matter masses, the annihilation into muons exhibits a slightly higher cross section than that into pion pairs, whereas the annihilation into electrons shows a comparatively steep rise. The variation of σ_{Ann} is shown in Fig. 10(b). It can be seen that annihilation into Standard Model particles is more prominent in the low velocity regions such as dwarf galaxies. However, its magnitude remains significantly smaller than that of σ_{BSF} . This indicates that when two dark matter particles attract each other, they are more likely to form a bound state rather than annihilate into Standard Model particles in dwarf galaxies. But due to presence of high dark photon flux in dwarf galaxies, the bound states would ionized, increasing the population of χ .

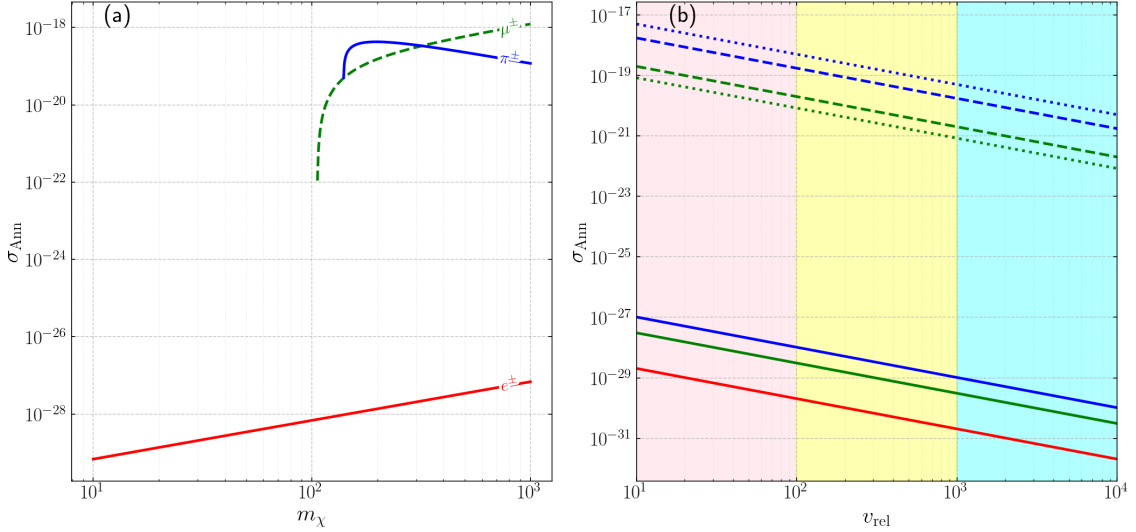


Figure 10: Panel (a) shows the annihilation of free dark matter cross section (for $v_{\text{rel}} = 3000$ km/s) as a function of the dark matter mass, varied from 0 to 1000 MeV. Panel (b) illustrates the dependence of σ_{Ann} on the relative velocity v_{rel} in km/s, where the red, green, and blue curves correspond to $m_\chi = 10$ MeV, 150 MeV, and 500 MeV, respectively. Solid, dashed, and dotted lines represent the annihilation of χ into e^\pm, μ^\pm and π^\pm , respectively.

In galaxy clusters, the small σ_{Ann} and σ_{BSF} , leads to a large population of free χ rather than SIMPonium bound states. At the galactic center, σ_{Ann} lies in a moderate range relative to the other two environments, while σ_{BSF} continues to dominate over σ_{Ann} , effectively reducing the abundance of free dark matter. However, the presence of a significant dark photon flux, together with the comparable magnitudes of σ_{BD} and σ_{BSF} , implies that SIMPonium can be ionized at nearly the same rate it is formed. .

5 Indirect detection

As discussed in the previous section, for Sub-GeV dark matter candidates the only kinematically accessible annihilation channels are $\chi\chi \rightarrow e^+e^-$, $\chi\chi \rightarrow \mu^+\mu^-$, and $\chi\chi \rightarrow \pi^+\pi^-$. We do not consider annihilation into neutral pion states, since the resulting signals are too faint to be detected by Sub-GeV telescopes [51]. In this section, we compute the photon flux produced from both the annihilation of dark matter and the decay of SIMPonium into visible particles. The differential gamma ray flux produced by dark matter annihilation is given by [52],

$$\frac{d\Phi_{\text{ann}}}{dE_\gamma d\Omega} = \frac{1}{8\pi m_\chi^2} \langle \sigma v \rangle_{\chi\chi \rightarrow f\bar{f}} \frac{dN_\gamma^f}{dE_\gamma} J(\theta), \quad (5.1)$$

where m_χ is the dark matter mass, $\langle \sigma v \rangle_{\chi\chi \rightarrow f\bar{f}}$ is the thermal averaged annihilation cross section of dark matter annihilation into the final state $f\bar{f}$, and dN_γ^f/dE_γ denotes the photon spectrum produced per annihilation in that channel.

For decaying dark matter, the corresponding expression is,

$$\frac{d\Phi_{\text{dec}}}{dE_\gamma d\Omega} = \frac{1}{4\pi m_\chi} \Gamma_{\chi \rightarrow f\bar{f}} \frac{dN_\gamma^f}{dE_\gamma} D(\theta), \quad (5.2)$$

where $\Gamma_{\chi \rightarrow f\bar{f}}$ is the decay rate of the dark matter particle.

The quantities $J(\theta)$ and $D(\theta)$ encode the astrophysical dependence of the signal through line-of-sight (l.o.s.) integrals over the dark matter density distribution $\rho(r)$,

$$J(\theta) = \int_{\text{l.o.s.}} \rho^2(r(s, \theta)) ds, \quad D(\theta) = \int_{\text{l.o.s.}} \rho(r(s, \theta)) ds, \quad (5.3)$$

where s is the distance along the line of sight, $\rho(r(s, \theta))$ is the dark matter density and a list numerical values of $J(\theta)$ and $D(\theta)$ is provided in Table 2 and for the analyses that follow, we use the $J(\theta)$ and $D(\theta)$ factors corresponding to the Milky Way galactic center, except where explicitly noted.

The term $\frac{dN_\gamma^f}{dE_\gamma}$ receives several contributions, such as inverse Compton scattering, final-state radiation, radiative decay, and bremsstrahlung emission. In this work, we focus on predicting the photon spectra arising from final state radiation and radiative decay,

$$\frac{dN_\gamma^f}{dE_\gamma} = \frac{dN_\gamma^f}{dE_\gamma} \Big|_{FSR} + \frac{dN_\gamma^f}{dE_\gamma} \Big|_{RD}.$$

Source	J-Factor ($\text{MeV}^2 \text{cm}^{-5}$)	D-Factor (MeV cm^{-2})
Milky Way galactic center	1.30×10^{29}	7.30×10^{26}
Draco dwarf	8.32×10^{24}	6.21×10^{21}
Coma cluster	1.99×10^{22}	3.69×10^{19}

Table 2: Annihilation J -factors and decay D -factors computed using the NFW density profile [53, 54].

5.1 Final-state radiation

The annihilation of free dark matter or decay of bound states into charged standard model particle produces photon via final state radiation and the resulting spectra due to leptonic final states is given by [55],

$$\frac{dN^{l^+l^-}}{dE_\gamma} \Big|_{FSR} = \frac{\alpha}{\pi\beta(3-\beta^2)m_\chi} \left[A \ln \frac{1+R(\nu)}{1-R(\nu)} - 2R(\nu)B \right], \quad (5.4)$$

where $l = e, \mu$, $A = \frac{(1+\beta^2)(3-\beta^2)}{\nu} - 2(3-\beta^2) + 2\nu$, $B = \frac{(1-\nu)(3-\beta^2)}{\nu} + \nu$, $\beta = 1 - 4\mu^2$, $\nu = E_\gamma/m_\chi$, $\mu = \frac{m_l}{2m_\chi}$, and $R(\nu) = \sqrt{1 - \frac{4\mu^2}{1-\nu}}$. Similarly FSR due to charged pions would be,

$$\frac{dN^{\pi^+\pi^-}}{dE_\gamma} = \frac{2\alpha}{\pi\beta m_\chi} \left[\left(\frac{\nu}{\beta^2} - \frac{1-\nu}{\nu} \right) R(\nu) + \left(\frac{1+\beta^2}{2\nu} - 1 \right) \ln \frac{1+R(\nu)}{1-R(\nu)} \right], \quad (5.5)$$

where ν, β and μ is the same as above with m_l replaced by m_π .

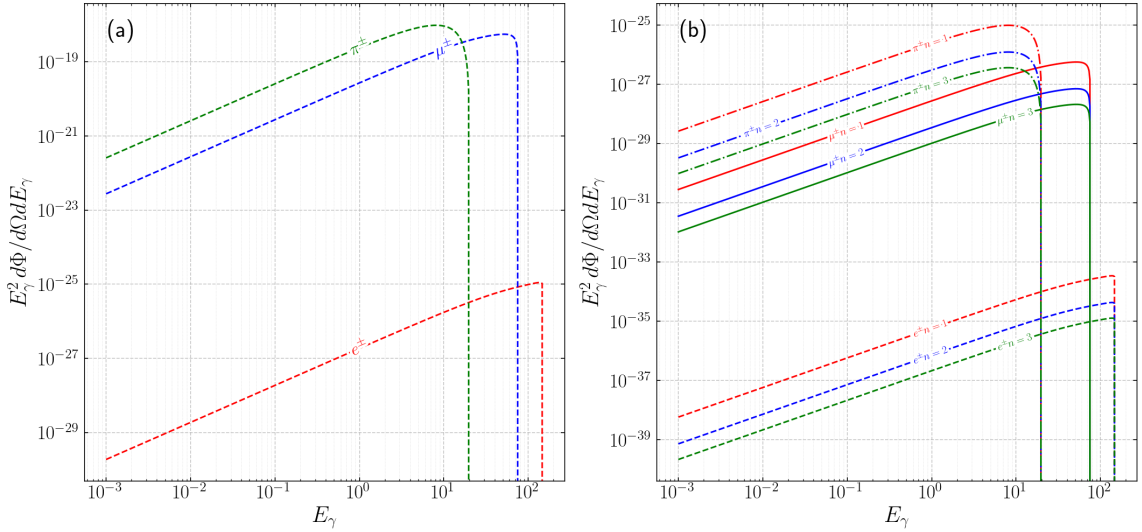


Figure 11: Panel (a) shows the final state radiation spectrum produced by charged leptons and pion which was product of annihilation of free χ as a function of energy of emitted photon in MeV. Panel (b) illustrates the FSR that was produced due to decay of SIMPonium into SM particles, where the red, green, and blue curves correspond to decay of $n = 1$, $n = 2$, and $n = 3$ states, respectively. Solid, dashed, and dotted lines represent the final SM particles as μ^\pm, e^\pm and π^\pm , respectively.

In Fig. 11(a), we show the differential flux of final state radiation produced by e^\pm , μ^\pm , and π^\pm . We consider a dark matter mass of $m_\chi = 150$ MeV and the differential flux produced by it exhibits a sharp cutoff at $E_\gamma^{\max} = m_\chi \left(1 - \frac{m_f^2}{m_\chi^2}\right)$, where $m_f = m_e, m_\mu, m_\pi$. Accordingly, the cutoff energies for e^\pm , μ^\pm , and π^\pm are approximately $E_\gamma^{\max} \simeq 149$ MeV, 75 MeV, and 20 MeV, respectively. Also it is clear that X-ray and soft gamma ray produced from pions and muons dominate the overall flux, while muon produce slightly energetic photons. Even if the photon flux produced by electrons are very small, they leave a distinctive feature by producing the most energetic gamma rays among all final states.

The FSR spectra arising from the decay of SIMPonium are shown in Fig. 11(b). We observe that the differential flux corresponding to visible decays are generally smaller than those produced by the annihilation of free χ particles. The photon energy cutoff follows a similar pattern as in the annihilation case, with $E_\gamma^{\max} = 149$ MeV, 75 MeV, 20 MeV for the three decay channels. Since the decay rate satisfies $\Gamma \propto |\psi_n(r=0)|^2$, the ground states decay more efficiently than the excited states. Similar to the flux produced due to annihilation the photon flux from bound state decay is also dominated by the FSR contributions from muons and pions.

While the results above correspond to $m_\chi = 150$ MeV, for $m_\chi < 110$ MeV the photon flux becomes very small, as only FSR from e^\pm is kinematically allowed, and this channel produces a comparatively weaker photon flux. In contrast, for more massive dark matter, the photon flux increases since heavier dark matter typically exhibits a larger annihilation

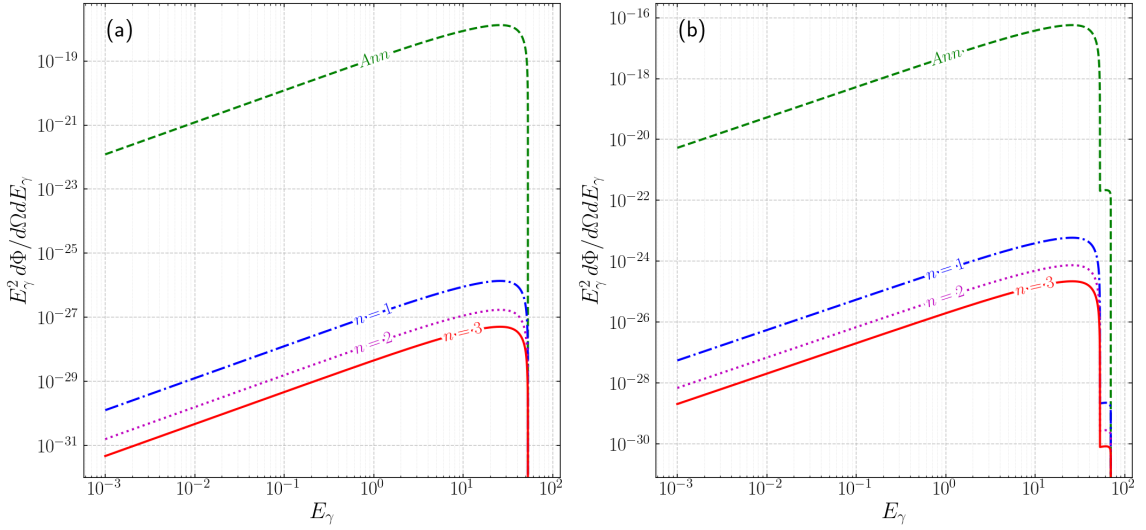


Figure 12: Panel (a) shows the radiative decay spectrum produced by decay of unstable muon as a function of energy of emitted photon in MeV. Panel (b) illustrates the total radiative decay spectrum combining the contribution from both muon and pion decay. In both panels the green, blue, purple and red curves correspond to annihilation of free dark matter and decay of $n = 1$, $n = 2$, and $n = 3$ states, respectively.

cross section σ_{Ann} , while the bound state formation cross section σ_{BSF} becomes smaller.

5.2 Radiative decay

When dark matter candidates annihilate or decay into an unstable Standard Model particle, the latter can subsequently produce photons through a radiative decay of the form $\text{SM} \rightarrow \text{SM} + \gamma$. For example, in the radiative decay of the muon, $\mu^- \rightarrow e^- \bar{\nu}_e \nu_\mu \gamma$, the resulting photon spectrum in muon's rest frame is given by [56],

$$\frac{dN_{\text{rad}}^\mu}{dE_\gamma} = \frac{\alpha(1-x)}{36\pi E_\gamma} \left[12(3 - 2x(1-x)^2) \log \frac{1-x}{r} + x(1-x)(46 - 55x) - 102 \right], \quad (5.6)$$

where, $x = \frac{2E_\gamma}{m_\mu}$ and $r = (\frac{m_e}{m_\mu})^2$. The differential flux produced by radiative decay of muons is shown in Fig. 12(a) and differential flux arising from the annihilation of free χ particles dominates over the flux produced by the decay of SIMPonium and the spectrum cutoff sharply at $E_\gamma^{\text{max}} \approx 75$ MeV.

Similarly, charged pions can produce photons through the radiative decay channel $\pi^- \rightarrow \ell^- \bar{\nu}_\ell \gamma$, and the corresponding photon spectrum is given by,

$$\frac{dN_{\text{rad}}^\pi}{dE_\gamma} = \frac{\alpha[f(x) + g(x)]}{24\pi m_\pi f_\pi^2 (r-1)^2 (x-1)^2 r x}, \quad (5.7)$$

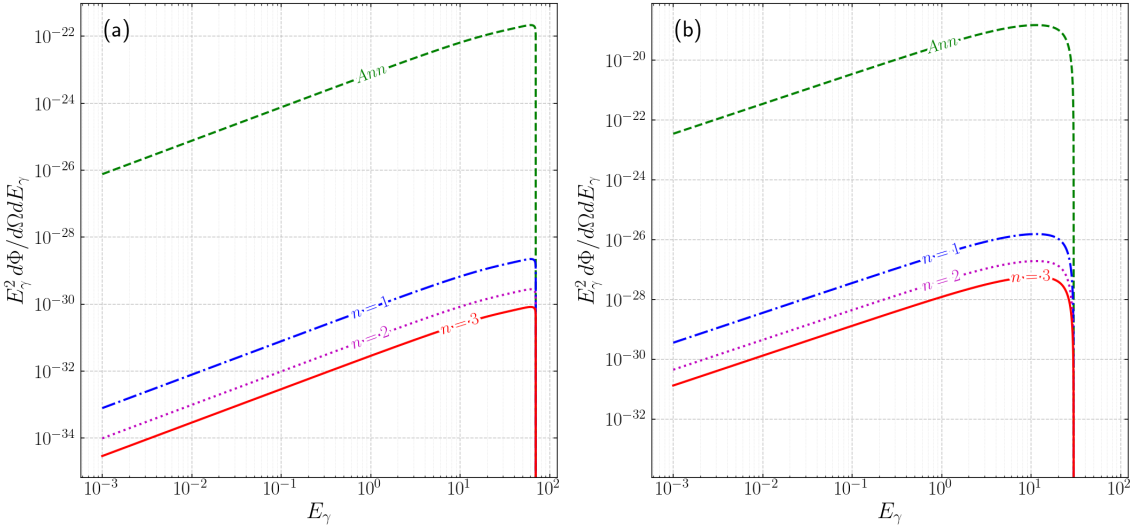


Figure 13: Panel (a) shows the radiative decay spectrum produced by decay of unstable pions decaying to electrons as a function of energy of emitted photon in MeV. Panel (b) illustrates radiative decay spectrum produced by decay of unstable pions decaying to muons. In both panels the green, blue, purple and red curves correspond to annihilation of free dark matter and decay of $n = 1$, $n = 2$, and $n = 3$ states, respectively.

where,

$$f(x) = (r + x + 1) \left[m_\pi^2 x^4 (F_A^2 + F_V^2) (r^2 - rx + r - 2(x-1)^2) - 12\sqrt{2} f_\pi m_\pi r (x-1) x^2 (F_A(r-2x+1) + x F_V) - 24 f_\pi^2 r (x-1) (4r(x-1) + (x-2)^2) \right], \quad (5.8)$$

$$g(x) = 12\sqrt{2} f_\pi r (x-1)^2 \log \left(\frac{r}{1-x} \right) \left[m_\pi x^2 (F_A(x-2r) - x F_V) + \sqrt{2} f_\pi (2r^2 - 2rx) - x^2 + 2x - 2 \right], \quad (5.9)$$

where $x = \frac{2E_\gamma}{m_\pi}$, $r = (\frac{m_l}{m_\pi})^2$ and f_π is pion decay constant, its value is 92.2 MeV. The axial and vector form factors are given by $F_A = 0.0119$ and $F_V(q^2) = F_V(0)(1 + aq^2)$ with $F_V(0) = 0.0254$, $a = 0.10$, $q = (1-x)$.

If the pion first decays into an on-shell muon, the resulting muon subsequently undergoes radiative decay and produces photons. Taking this possibility into account, the total photon spectrum arising from pion decay is,

$$\frac{dN_{\text{RadTot}\gamma}^\pi}{dE_\gamma} \Big|_{E_\pi=m_\pi} = \sum_{\ell=e, \mu} \text{BR}(\pi \rightarrow \ell \nu_\ell) \frac{dN_{\text{Rad}\gamma}^\pi}{dE_\gamma} \Big|_{E_\pi=m_\pi} + \text{BR}(\pi \rightarrow \mu \nu_\mu) \frac{dN_{\text{Rad}\gamma}^\mu}{dE_\gamma} \Big|_{E_\mu=E_\pi}, \quad (5.10)$$

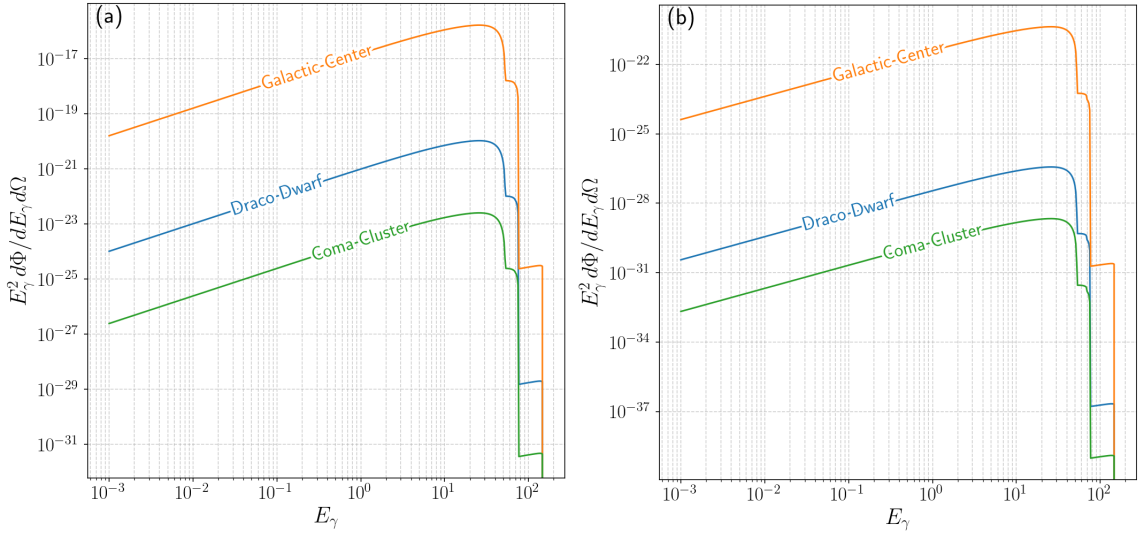


Figure 14: Panel(a) and (b) shows the combination of final state radiation and radiative decay spectra for free χ and decay SIMPonium respectively.

where E_π and E_* represent the pion and muon energies in the pion rest frame.

The two separate contributions ($l = e, \mu$) corresponding to the first term in Eq. (5.10) are shown in Figs. 13(a) and (b) and since $\text{BR}(\pi \rightarrow \mu\nu_\mu) \approx 0.98$ the second term is identical to the radiative decay from muons as shown in Fig. 12(a). And due to this high branching ratio, photon production during pion decay into muons dominates over the electron channel. The maximum photon energy during radiative decay is determined by $E_\gamma^{\max} = \frac{m_\pi^2 - m_f^2}{2m_\pi}$, where $f = e, \mu$. Using this, we estimate the maximum photon energies for pion decays into muons and electrons as $E_\gamma^{\max} \simeq 74$ and 35 MeV, respectively.

Fig. 12 (b) shows the complete radiative decay spectrum obtained by combining the contributions from both muon decay and pion decay. It is evident that the differential flux is dominated by muon decay and the muonic decay channel of the pion. It is also notable that the photon flux produced by radiative decay is greater than that produced by final-state radiation. Similar to the FSR spectrum, the radiative decay spectrum decreases drastically for $m_\chi < 100$ MeV due to kinematic suppression, while for heavier dark matter the photon flux increases owing to the larger annihilation cross section σ_{ann} .

5.3 Full spectrum

To investigate the sensitivity of the differential photon flux to different astrophysical targets, we adopt the J-factor and D-factor values specified in Table 2. Substituting these into Eq. (5.1) and Eq. (5.2) allows for a systematic study of the flux variations in diverse environments. These results are shown in Figs. 14(a) and (b), where we present the differential flux produced by the annihilation of free dark matter and by the decay of bound states, including contributions from both the radiative decay spectrum and final-state radiation (FSR), for various regions such as the galactic center, dwarf galaxies, and galaxy clusters. Furthermore, since the spectrum produced by annihilation exceeds that from SIMPonium

decay, Fig. 14(a) represents the total photon spectrum predicted by this model and it is evident that photon flux produced by these are feeble could not be be detected by indirect experimental searches .

From Fig. 14(a), we can see that most of the photon would be produced in range of hard x-ray to soft gamma ray dominated by radiative decay of muons with $E_{\gamma}^{max} \approx 75\text{MeV}$. And flux of photons produced by final state radiation of electrons with $E_{\gamma}^{max} \approx 149\text{MeV}$ would be lesser compared to former case. Owing to the higher dark matter density, the Galactic Center produces a larger flux of photons. As discussed in the previous section, lighter dark matter with $m_{\chi} = 150$ MeV can form bound states efficiently. However, since these bound states are short-lived and can decay into dark radiation, the population of free dark matter particles would gradually deplete through bound-state formation and subsequent decay. This process could potentially explain the lack of experimental evidence for dark matter annihilation signals, as the number of annihilating free χ particles would be reduced. Although the Galactic Center exhibits a strong photon flux, the high astrophysical background makes it challenging to distinguish dark matter induced signals from the background emission. Even though the annihilation rate of free dark matter is highest in low-velocity regions such as dwarf galaxies, we typically have $\sigma_{\text{Ann}} \approx \sigma_{\text{BSF}}$ for heavier dark matter. Consequently, the number of free χ which would produce a visible signal is also reduced, and bound states would rather decay into dark radiation rather than visible ones. Furthermore, the signals from these sources are much fainter than those from the Galactic Center due to their larger distances from Earth, but their lack of background noise makes it as a viable candidate. Despite being a large structure, the signals produced by galaxy clusters are weaker compared to those from the galactic center and dwarf galaxies, primarily due to their large distances from Earth and the presence of significant background noise. In these regions, σ_{Ann} is relatively small, resulting in a lower overall photon flux. Due to lower σ_{BSF} and high Γ_{Dec} the small portion of SIMPonium would decay into dark radiation, further suppressing the photon signals arising from visible decay channels. Consequently, most of the observable signals from galaxy clusters would originate from the annihilation of free dark matter.

6 Conclusion

In this work, we have shown that bound-state formation slightly reduces the abundance of free dark matter. Due to the presence of bound states, the final dark matter abundance is determined primarily by number-changing processes involving initial bound states, rather than by the conventional $4\chi \rightarrow 2\chi$ annihilation channel. The freeze out of free dark matter and SIMPonium bound states occurs at $x_f \approx 20$ and $x_f \approx 250$, respectively. This late freeze-out of bound states leads to a significantly smaller present-day abundance of SIMPonium compared to free dark matter.

We have studied the influence of bound states on three major astrophysical regions: galaxy clusters, the galactic center, and dwarf galaxies. Since $\Gamma_{\text{B}_n} > \sigma_{\text{BSF}}$ and Γ_{Trans} is approximately the same across these regions, we expect that most of the bound states would decay into pure dark radiation, with the surviving bound states primarily in the ground

state. At the galactic clusters, we find that bound states are less frequently formed, which reduces the population of dark photons produced via SIMPonium decay. However, these bound states are efficiently ionized, and since σ_{ann} is also small, we expect the total dark sector population to be dominated by free dark matter. In contrast, in low velocity regions such as dwarf galaxies, both σ_{BSF} and σ_{Ann} are relatively large and the enhanced presence of dark photons produced by bound-state decay facilitates more frequent ionization. Consequently, the population of free dark matter is expected to be smaller than in galaxy clusters, while the abundances of bound states and dark photons are slightly higher. For galactic center, both σ_{BSF} and σ_{Ann} take moderate values compared to the other regions, leading to intermediate populations of free χ , bound states, and dark photons.

The indirect detection study shows that lighter dark matter candidates ($m_\chi < 110$ MeV) produce a much weaker photon spectrum compared to heavier dark matter. The annihilation of free dark matter generates a higher photon flux than the decay of SIMPonium into Standard Model particles, and the photon flux from excited state decays is even smaller. We also analyzed the total photon spectrum across the three astrophysical regions discussed above, and in all cases, the spectrum produced by the radiative decay of Standard Model particles dominates over the contribution from final state radiation. Among the radiative decay channels, decays involving muons yield the highest photon flux. However, the photon spectra predicted in this model remain below the detection thresholds of current sub-GeV telescopes such as the *INTEGRAL* X-ray telescope. Therefore, this scenario could provide a plausible explanation for the lack of observed indirect signals of dark matter.

A Coulomb wavefunctions

A.1 Bound state wavefunction

For a two body system interacting via an attractive Coulomb potential $V(r) = -V_0/r$, the radial Schrödinger equation describing the relative motion in the center of mass frame (with $\hbar = 1$) takes the form given by Eq. A.1. We first derive the solutions corresponding to the bound states of this system,

$$\frac{d^2R(r)}{dr^2} + \frac{2}{r} \frac{dR(r)}{dr} + 2\mu[E + \frac{V_0}{r} - \frac{l(l+1)}{2\mu r^2}]R(r) = 0. \quad (\text{A.1})$$

Substituting $r = s$ and $R(r) = \psi(s)$ the above equation simplifies as,

$$\frac{d^2\psi(s)}{ds^2} + \frac{2}{s} \frac{d\psi(s)}{ds} + \frac{1}{s^2}[-\alpha s^2 + \beta s - \gamma] = 0, \quad (\text{A.2})$$

where $\alpha = -2\mu E$, $\beta = 2\mu V_0$ and $\gamma = l(l+1)$.

Following the Nikiforov–Uvarov method to solve this differential equation, we obtain the radial wavefunction in the form,

$$R(r) = N_{nlm} r^l e^{-\sqrt{\alpha}r} L_n^{2l+1}(2r\sqrt{\alpha}), \quad (\text{A.3})$$

where $L_n^{2l+1}(2r\sqrt{\alpha})$ is the associated laguerre polynomial and the complete wave function is given by,

$$\psi(r) = R(r)Y_m^l, \quad (\text{A.4})$$

and the energy eigenvalues are given by,

$$E_n = \frac{-V_0^2 \mu}{2n^2}. \quad (\text{A.5})$$

A.2 Scattering state wavefunction

To describe the scattering states, we use the relation,

$$E = \frac{k^2}{2\mu} = \frac{\mu v^2}{2},$$

and the Schrödinger equation for the Coulomb interaction can be written as,

$$\left[\nabla^2 + k^2 - \frac{2\delta k}{rv} \right] \psi(\mathbf{r}) = 0, \quad (\text{A.6})$$

where $\delta = \frac{V_0}{v}$ and $k = \mu v$. Using the ansatz $\psi(\mathbf{r}) = e^{ikz} f(r - z)$ and defining the variable $u = r - z$, the equation simplifies to,

$$u \frac{d^2 f(u)}{du^2} + (1 - iku) \frac{df(u)}{du} + \delta k f(u) = 0. \quad (\text{A.7})$$

This equation is of the confluent hypergeometric type, and its solution can therefore be written in the form,

$$\psi(r) = N e^{ikr} F[-i\delta; 1; i(kr - k.r)] \quad (\text{A.8})$$

B Perturbative matrix elements

B.1 Matrix elements for σ_{BSF} and Γ_{Trans}

The Feynman diagrams for the process $\chi(p_1) + \chi^*(p_2) \rightarrow \chi(k_1) + \chi^*(k_2) + A^\mu(Q)$, which contribute to the matrix elements relevant for the bound-state formation cross section σ_{BSF} and the transition rate Γ_{Trans} are shown in Fig. 15. The corresponding matrix elements are given below,

$$\begin{aligned} M_1 &= \frac{2k_1 \cdot \epsilon^*(Q) + Q \cdot \epsilon^*(Q)}{2k_1 \cdot Q + m_\chi^2}, \\ M_2 &= \frac{-2k_2 \cdot \epsilon^*(Q) + Q \cdot \epsilon^*(Q)}{2k_2 \cdot Q + m_\chi^2}, \\ M_3 &= \frac{g_\chi^3 (p_1 - p_2)_\mu g^{\mu\nu} (k_1 - k_2 - Q)_\nu (-2k_2 - Q)^\beta \epsilon_\beta^*(Q)}{s[(k_2 + Q)^2 - m_\chi^2]}, \\ M_4 &= \frac{g_\chi^3 (p_1 - p_2)_\mu g^{\mu\nu} (k_1 - k_2 + Q)_\nu (2k_1 + Q)^\beta \epsilon_\beta^*(Q)}{s[(k_1 + Q)^2 - m_\chi^2]}, \\ M_5 &= \frac{g_\chi^3 (p_1 - p_2)_\mu g^{\mu\nu} g^{\nu\beta} \epsilon_\beta^*(Q)}{s}, \\ M_6 &= \frac{g_\chi^3 (p_1 + k_1)_\mu g^{\mu\nu} (-p_2 - k_2 - Q)_\nu (-2k_2 - Q)^\beta \epsilon_\beta^*(Q)}{t[(k_2 + Q)^2 - m_\chi^2]}, \end{aligned}$$

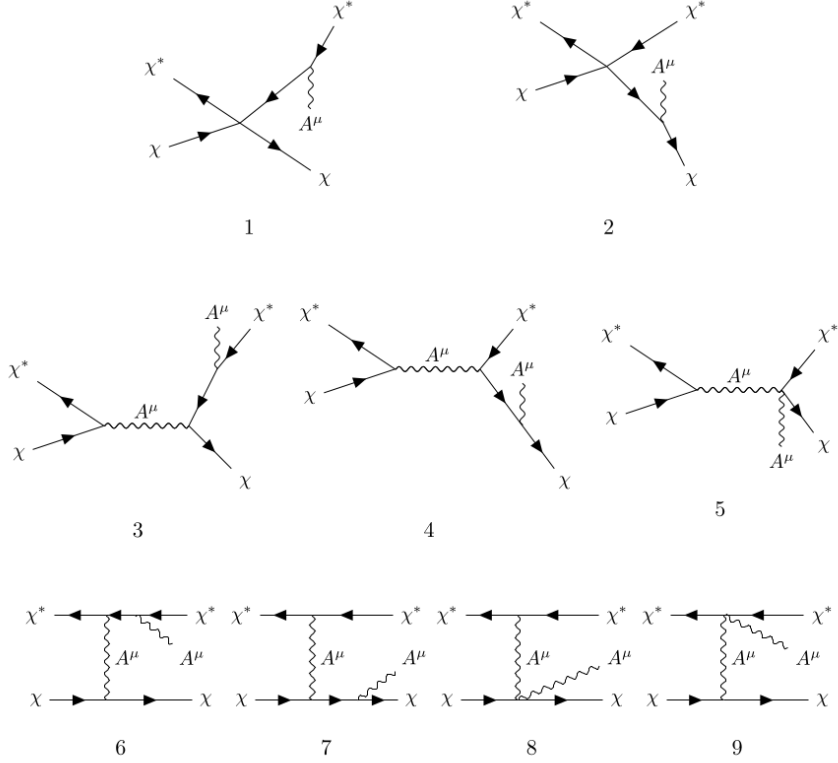


Figure 15: Feynman diagrams contributing for σ_{BSF} and Γ_{Trans}

$$\begin{aligned}
 M_7 &= \frac{g_\chi^3 (p_1 + k_1 + Q)_\mu g^{\mu\nu} (-p_2 - k_2)_\nu (2k_2 + Q)^\beta \epsilon_\beta^*(Q)}{t[(k_1 + Q)^2 - m_\chi^2]}, \\
 M_8 &= \frac{g_\chi^3 (p_1 + k_1)_\mu g^{\mu\nu} g^{\nu\beta} \epsilon_\beta^*(Q)}{t}, \\
 M_9 &= \frac{g_\chi^3 (-p_2 - k_2)_\mu g^{\mu\nu} g^{\nu\beta} \epsilon_\beta^*(Q)}{t}.
 \end{aligned}$$

And the total matrix element would be the sum of all nine matrix elements,

$$M = M_1 + M_2 + M_3 + M_4 + M_5 + M_6 + M_7 + M_8 + M_9. \quad (\text{B.1})$$

In the rest frame of the bound state, the constituent four-momenta are,

$$k_1^\mu = (E, \mathbf{k}), \quad k_2^\mu = (E, -\mathbf{k}).$$

The squared matrix element is evaluated using the transversality condition on the physical polarization vectors,

$$k_\mu \epsilon^\mu(k, \lambda) = 0,$$

together with the standard polarization sum,

$$\sum_{\lambda} \epsilon_{\mu}^*(k, \lambda) \epsilon_{\nu}(k, \lambda) = -g_{\mu\nu}.$$

This leads to the polarization summed squared amplitude,

$$\sum_{\lambda} |M|^2 = -g^{\mu\nu} M_{\mu}^* M_{\nu}, \quad (\text{B.2})$$

where M_{μ} denotes the matrix element before contraction with the polarization vector.

B.2 Matrix elements for Γ_{B_n} and σ_{Ann}

The matrix element governing the decay of the SIMPonium bound state is obtained from the Feynman diagram shown below and can be written as $M = 2g_{\chi}^2$.

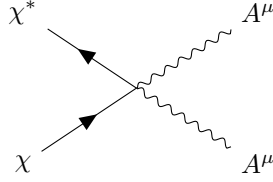


Figure 16: Feynman diagram contributing to decay of bound state.

Similarly the feynman diagram contributing for annihilation of dark matter is shown below.

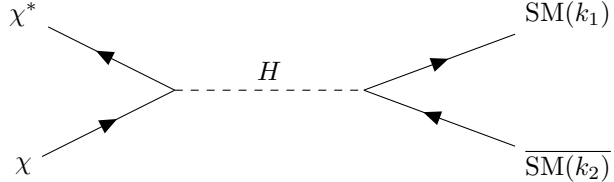


Figure 17: Feynman diagram contributing to annihilation of dark matter.

The matrix element for dark matter annihilation into a pair of light leptons f is given by,

$$M = \frac{\lambda_{\chi H} m_f}{2} \frac{\bar{u}(k_1) v(k_2)}{s - m_h^2}.$$

Using trace techniques, the squared matrix element is,

$$|M|^2 = \frac{\lambda_{\chi H}^2 m_f^2}{4} \frac{s - 4m_f^2}{(s - m_h^2)^2}. \quad (\text{B.3})$$

Within chiral perturbation theory, the matrix element for dark matter annihilation into pions is,

$$M = \frac{\lambda_{\chi H} m_{\pi}^2}{2} \frac{1}{s - m_h^2}. \quad (\text{B.4})$$

C Calculation of thermal average cross sections

C.1 $4\chi \rightarrow 2\chi$ annihilation cross sections

We derive the thermally averaged cross section for the process $4\chi \rightarrow 2\chi$. Consider the process,

$$\chi^*(p_1) + \chi^*(p_2) + \chi(p_3) + \chi(p_4) \rightarrow \chi(p_5) + \chi(p_6).$$

The thermal average cross section for this process would be given by,

$$\begin{aligned} \langle \sigma v^3 \rangle_C &= \frac{1}{n_1^{\text{eq}} n_2^{\text{eq}} n_3^{\text{eq}} n_4^{\text{eq}}} \int \frac{g_\chi d^3 p_1}{(2\pi)^3 2E_1} \frac{g_\chi d^3 p_2}{(2\pi)^3 2E_2} \frac{g_\chi d^3 p_3}{(2\pi)^3 2E_3} \frac{g_\chi d^3 p_4}{(2\pi)^3 2E_4} \frac{g_\chi d^3 p_5}{(2\pi)^3 2E_5} \frac{g_\chi d^3 p_6}{(2\pi)^3 2E_6} \\ &\quad \times (2\pi)^4 \delta^4(p_1 + p_2 + p_3 - p_4 - p_5) |\mathcal{M}|^2 f_1^{\text{eq}} f_2^{\text{eq}} f_3^{\text{eq}} f_4^{\text{eq}}, \\ &= \frac{1}{n_1^{\text{eq}} n_2^{\text{eq}} n_3^{\text{eq}} n_4^{\text{eq}}} \int \frac{g_\chi d^3 p_1}{(2\pi)^3 2E_1} \frac{g_\chi d^3 p_2}{(2\pi)^3 2E_2} \frac{g_\chi d^3 p_3}{(2\pi)^3 2E_3} \frac{g_\chi d^3 p_4}{(2\pi)^3 2E_4} (\sigma v^3)_C f_1^{\text{eq}} f_2^{\text{eq}} f_3^{\text{eq}} f_4^{\text{eq}}. \end{aligned} \quad (\text{C.1})$$

We know that the number density at equilibrium would be given by,

$$n_i^{\text{eq}} = \frac{g_i}{(2\pi)^3} \int d^3 p f_i^{\text{eq}}.$$

Since dark matter is a cold species $f_i^{\text{eq}} = e^{\frac{-E_i}{T_i}}$ and the number density will be,

$$n_i^{\text{eq}} = \frac{g_i}{(2\pi)^3} 4\pi m_i^2 T K_2(m_i/T),$$

where $K_2(m_i/T)$ is the Bessel function of second kind. Substituting these in Eq. (C.1) we get,

$$\langle \sigma v^3 \rangle_C = \left(\frac{K_1(m_\chi/T)}{K_2(m_\chi/T)} \right)^4 (\sigma v)_C. \quad (\text{C.2})$$

The SIMPonium bound state in the final state is formed via the process,

$$\chi^*(p_1) + \chi^*(p_2) + \chi(p_3) + \chi(p_4) \rightarrow B_n(p_5) + A^\mu(p_6).$$

The thermally averaged cross section is then given by,

$$\begin{aligned} \langle \sigma v^3 \rangle_D &= \frac{1}{n_1^{\text{eq}} n_2^{\text{eq}} n_3^{\text{eq}} n_4^{\text{eq}}} \sqrt{\frac{2}{\mu}} \int \frac{g_\chi d^3 p_1}{(2\pi)^3 2E_1} \frac{g_\chi d^3 p_2}{(2\pi)^3 2E_2} \frac{g_\chi d^3 p_3}{(2\pi)^3 2E_3} \frac{g_\chi d^3 p_4}{(2\pi)^3 2E_4} \frac{g_{B_n} d^3 p_5}{(2\pi)^3 2E_5} \frac{g_{A^\mu} d^3 p_6}{(2\pi)^3 2E_6} \\ &\quad \times \frac{d^3 P}{(2\pi)^3} \frac{d^3 Q}{(2\pi)^3} (2\pi)^4 \delta^4(p_1 + p_2 + p_3 - p_4 - p_5) |\psi_s(P)|^2 |\psi_n(Q)|^2 |\mathcal{M}^{\text{feyn}}|^2 f_1^{\text{eq}} f_2^{\text{eq}} f_3^{\text{eq}} f_4^{\text{eq}}, \\ &= \frac{1}{n_1^{\text{eq}} n_2^{\text{eq}} n_3^{\text{eq}} n_4^{\text{eq}}} \int \frac{g_\chi d^3 p_1}{(2\pi)^3 2E_1} \frac{g_\chi d^3 p_2}{(2\pi)^3 2E_2} \frac{g_\chi d^3 p_3}{(2\pi)^3 2E_3} \frac{g_\chi d^3 p_4}{(2\pi)^3 2E_4} (\sigma v^3)_D f_1^{\text{eq}} f_2^{\text{eq}} f_3^{\text{eq}} f_4^{\text{eq}}, \\ \langle \sigma v^3 \rangle_D &= \left(\frac{K_1(m_\chi/T)}{K_2(m_\chi/T)} \right)^4 (\sigma v)_D. \end{aligned} \quad (\text{C.3})$$

Even though Eq. (C.2) and Eq. (C.3) have similar structure, the presence of final bound state formation will alter $(\sigma v^3)_D$ cross section. It is also possible that a previously formed

bound state interacts via a four-point vertex and contributes to the total ($4\chi \rightarrow 2\chi$) annihilation rate. One such process is,

$$\chi^*(p_1) + \chi^*(p_2) + B_n(p_3) \rightarrow \chi^*(p_4) + \chi(p_5).$$

The corresponding thermal average cross section would be,

$$\begin{aligned} \langle \sigma v^2 \rangle_E &= \frac{1}{n_1^{\text{eq}} n_2^{\text{eq}} n_3^{\text{eq}}} \sqrt{\frac{2}{\mu}} \int \frac{g_\chi d^3 p_1}{(2\pi)^3 2E_1} \frac{g_\chi d^3 p_2}{(2\pi)^3 2E_2} \frac{g_{B_n} d^3 p_3}{(2\pi)^3 2E_3} \frac{g_\chi d^3 p_4}{(2\pi)^3 2E_4} \frac{g_\chi d^3 p_5}{(2\pi)^3 2E_5} \\ &\quad \times \frac{d^3 Q}{(2\pi)^3} (2\pi)^4 \delta^4(p_1 + p_2 + p_3 - p_4 - p_5) |\psi_n(Q)|^2 |\mathcal{M}^{\text{feyn}}|^2 f_1^{\text{eq}} f_2^{\text{eq}} f_3^{\text{eq}} f_4^{\text{eq}} f_5^{\text{eq}}, \\ &= \frac{1}{n_1^{\text{eq}} n_2^{\text{eq}} n_3^{\text{eq}}} \int \frac{g_\chi d^3 p_1}{(2\pi)^3 2E_1} \frac{g_\chi d^3 p_2}{(2\pi)^3 2E_2} \frac{g_{B_n} d^3 p_3}{(2\pi)^3 2E_3} (\sigma v^2)_E f_1^{\text{eq}} f_2^{\text{eq}} f_3^{\text{eq}}, \\ \langle \sigma v^2 \rangle_E &= \left(\frac{K_1(m_\chi/T)}{K_2(m_\chi/T)} \right)^2 \frac{K_1(M_{B_n}/T)}{K_2(M_{B_n}/T)} (\sigma v)_E. \end{aligned} \quad (\text{C.4})$$

Furthermore, two incoming SIMPonium bound states can annihilate into free dark matter particles, as shown below,

$$B_n(p_1) B_n(p_2) \rightarrow \chi(p_3) \chi(p_4).$$

The thermal average cross section would be,

$$\begin{aligned} \langle \sigma v \rangle_F &= \frac{1}{n_1^{\text{eq}} n_2^{\text{eq}}} \frac{2}{\mu} \int \frac{g_{B_n} d^3 p_1}{(2\pi)^3 2E_1} \frac{g_{B_n} d^3 p_2}{(2\pi)^3 2E_2} \frac{g_\chi d^3 p_3}{(2\pi)^3 2E_3} \frac{g_\chi d^3 p_4}{(2\pi)^3 2E_4} \\ &\quad \times \frac{d^3 P}{(2\pi)^3} \frac{d^3 Q}{(2\pi)^3} (2\pi)^4 \delta^4(p_1 + p_2 + p_3 - p_4 - p_5) |\psi_n(P)|^2 |\psi_n(Q)|^2 |\mathcal{M}^{\text{feyn}}|^2 f_1^{\text{eq}} f_2^{\text{eq}} f_3^{\text{eq}} f_4^{\text{eq}}, \\ &= \frac{1}{n_1^{\text{eq}} n_2^{\text{eq}}} \int \frac{g_{B_n} d^3 p_1}{(2\pi)^3 2E_1} \frac{g_{B_n} d^3 p_2}{(2\pi)^3 2E_2} (\sigma v)_F f_1^{\text{eq}} f_2^{\text{eq}}, \\ \langle \sigma v \rangle_F &= \left[\frac{K_1(M_{B_n}/T)}{K_2(M_{B_n}/T)} \right]^2 (\sigma v)_F. \end{aligned} \quad (\text{C.5})$$

Another related process is,

$$\chi^*(p_1) + \chi^*(p_2) + B_n(p_3) \rightarrow B_n(p_4) + A^\mu(p_5).$$

The thermally averaged cross section for this process is evaluated as follows,

$$\begin{aligned} \langle \sigma v^2 \rangle_G &= \frac{1}{n_1^{\text{eq}} n_2^{\text{eq}} n_3^{\text{eq}}} \left(\frac{2}{\mu} \right)^{3/2} \int \frac{g_\chi d^3 p_1}{(2\pi)^3 2E_1} \frac{g_\chi d^3 p_2}{(2\pi)^3 2E_2} \frac{g_{B_n} d^3 p_3}{(2\pi)^3 2E_3} \frac{g_{B_n} d^3 p_4}{(2\pi)^3 2E_4} \frac{g_{A^\mu} d^3 p_5}{(2\pi)^3 2E_5} \\ &\quad \times \frac{d^3 P}{(2\pi)^3} \frac{d^3 K}{(2\pi)^3} \frac{d^3 Q}{(2\pi)^3} (2\pi)^4 \delta^4(p_1 + p_2 - p_3 - p_4) |\psi_n(Q)|^2 |\psi_s(K)|^2 |\psi_n(P)|^2 |\mathcal{M}^{\text{feyn}}|^2 \\ &\quad \times f_1^{\text{eq}} f_2^{\text{eq}} f_3^{\text{eq}} f_4^{\text{eq}} f_5^{\text{eq}}, \\ &= \frac{1}{n_1^{\text{eq}} n_2^{\text{eq}} n_3^{\text{eq}}} \int \frac{g_\chi d^3 p_1}{(2\pi)^3 2E_1} \frac{g_\chi d^3 p_2}{(2\pi)^3 2E_2} \frac{g_{B_n} d^3 p_3}{(2\pi)^3 2E_3} (\sigma v^2)_G f_1^{\text{eq}} f_2^{\text{eq}} f_3^{\text{eq}}, \end{aligned}$$

$$\langle \sigma v^2 \rangle_G = \left(\frac{K_1(m_\chi/T)}{K_2(m_\chi/T)} \right)^2 \frac{K_1(M_{B_n}/T)}{K_2(M_{B_n}/T)} (\sigma v^2)_G. \quad (\text{C.6})$$

The presence of the four point interaction term $|\chi|^4$ also allows bound states to undergo number changing processes such as,

$$B_n(p_1)B_n(p_2) \rightarrow B_n(p_3)A^\mu(p_4),$$

$$\begin{aligned} \langle \sigma v \rangle_H &= \frac{1}{n_1^{\text{eq}} n_2^{\text{eq}}} \left(\frac{2}{\mu} \right)^{3/2} \int \frac{g_{B_n} d^3 p_1}{(2\pi)^3 2E_1} \frac{g_{B_n} d^3 p_2}{(2\pi)^3 2E_2} \frac{g_{B_n} d^3 p_3}{(2\pi)^3 2E_3} \frac{g_{A^\mu} d^3 p_4}{(2\pi)^3 2E_4} \\ &\times \frac{d^3 P}{(2\pi)^3} \frac{d^3 K}{(2\pi)^3} \frac{d^3 Q}{(2\pi)^3} (2\pi)^4 \delta^4(p_1 + p_2 - p_3 - p_4) |\psi_n(Q)|^2 |\psi_s(K)|^2 |\psi_n(P)|^2 |\mathcal{M}^{\text{feyn}}|^2 \\ &\times f_1^{\text{eq}} f_2^{\text{eq}} f_3^{\text{eq}} f_4^{\text{eq}}, \\ &= \frac{1}{n_1^{\text{eq}} n_2^{\text{eq}}} \int \frac{g_\chi d^3 p_1}{(2\pi)^3 2E_1} \frac{g_{B_n} d^3 p_2}{(2\pi)^3 2E_2} (\sigma v^2)_H f_1^{\text{eq}} f_2^{\text{eq}}, \\ \langle \sigma v \rangle_H &= \left(\frac{K_1(M_{B_n}/T)}{K_2(M_{B_n}/T)} \right)^2 (\sigma v)_H. \end{aligned} \quad (\text{C.7})$$

C.2 Bound state dynamics cross sections

The thermal average cross section for bound state formation process $\chi(p_1)\chi(p_2) \rightarrow B_n(p_3)A^\mu(p_4)$ will be,

$$\langle \sigma v \rangle_A = \frac{1}{n_1^{\text{eq}} n_2^{\text{eq}}} \int \frac{g_\chi d^3 p_1}{(2\pi)^3 2E_1} \frac{g_\chi d^3 p_2}{(2\pi)^3 2E_2} \frac{g_B d^3 p_3}{(2\pi)^3 2E_3} \frac{g_{A^\mu} d^3 p_4}{(2\pi)^3 2E_4} (2\pi)^4 \delta^4(p_1 + p_2 - p_3 - p_4) |M|^2 f_1^{\text{eq}} f_2^{\text{eq}},$$

Wwhich would simplify as,

$$\langle \sigma v \rangle_A = \frac{1}{n_1^{\text{eq}} n_2^{\text{eq}}} \int \frac{g_\chi d^3 p_1}{(2\pi)^3} \frac{g_\chi d^3 p_2}{(2\pi)^3 2E_2} (\sigma v)_{BSF} f_1^{\text{eq}} f_2^{\text{eq}}, \quad (\text{C.8})$$

$$\langle \sigma v \rangle_A = \left(\frac{K_1(m_\chi/T)}{K_2(m_\chi/T)} \right)^2 (\sigma v)_{BSF}. \quad (\text{C.9})$$

The thermally averaged decay of bound state $B_n(p_1) \rightarrow A^\mu(p_2) + A^\mu(p_3)$ is given by,

$$\langle \Gamma \rangle_I = \frac{1}{n_{B_n}^{\text{eq}}} \int \frac{g_{B_n} d^3 p_1}{(2\pi)^3} \Gamma_I f_1^{\text{eq}}, \quad (\text{C.10})$$

which can be evaluated analytically as

$$\langle \Gamma \rangle_I = \left(\frac{K_1(m_{B_n}/T)}{K_2(m_{B_n}/T)} \right) \Gamma_I. \quad (\text{C.11})$$

The thermally averaged deexcitation rate of excited bound states $B_{n'}(p_1) \rightarrow B_n(p_2) + A^\mu(p_3)$ is given by,

$$\langle \Gamma \rangle_J = \frac{1}{n_{B_{n'}}^{\text{eq}}} \int \frac{g_{B_{n'}} d^3 p_1}{(2\pi)^3} \Gamma_I f_1^{\text{eq}}, \quad (\text{C.12})$$

which can be evaluated analytically as,

$$\langle \Gamma \rangle_J = \left(\frac{K_1(m_{B_{n'}}/T)}{K_2(m_{B_{n'}}/T)} \right) \Gamma_J. \quad (\text{C.13})$$

In the previous calculations, we employed the formal method to obtain the thermally averaged cross section. Here, we illustrate a simpler approach by considering the SIMPo-nium ionization process: $B_n(p_1)A^\mu(p_2) \rightarrow \chi(p_3)\chi(p_4)$, for which the thermal average cross section is given by,

$$\langle \sigma v \rangle_B = \frac{x^{3/2}}{2\sqrt{\pi}} \int_0^\infty dv v^2 e^{-\frac{xv^2}{4}} (\sigma v)_{BD}. \quad (\text{C.14})$$

The thermal average cross section for annihilation of free χ into a pair of SM particles has a standard result given by,

$$\langle \sigma v \rangle_{Ann} = \frac{x}{16T m_\chi^4 K_2^2(x)} \int_0^\infty ds (\sigma v)_{Ann} K_1\left(\frac{\sqrt{s}}{T}\right) s \sqrt{s - 4m_\chi^2}. \quad (\text{C.15})$$

References

- [1] N. Aghanim et al., *Planck 2018 results - VI. Cosmological parameters*, *Astron. Astrophys.* **641** (2020) A6.
- [2] T. Abe, M. Kakizaki, S. Matsumoto and O. Seto, *Vector WIMP miracle*, *Phys. Lett. B* **713** (2012) 211.
- [3] E. Aprile et al., *Dark matter results from 100 live days of XENON100 data*, *Phys. Rev. Lett.* **107** (2011) 131302.
- [4] D.S. Akerib et al., *First results from the LUX dark matter experiment at the Sanford Underground Research Facility*, *Phys. Rev. Lett.* **112** (2014) 091303.
- [5] Y. Meng et al., *Dark matter search results from the PandaX-4T commissioning run*, *Phys. Rev. Lett.* **127** (2021) 261802.
- [6] S. Lowette et al., *Search for dark matter at CMS*, *Nucl. Part. Phys. Proc.* **273** (2016) 503.
- [7] D. Abercrombie et al., *Dark matter benchmark models for early LHC run-2 searches: report of the ATLAS/CMS dark matter forum*, *Phys. Dark Univ.* **27** (2020) 100371.
- [8] S. Schramm, *Searching for dark matter with the ATLAS detector*, Springer, Cham (2016).
- [9] D. Horns et al., *Indirect search for Dark Matter with HESS*, *Adv. Space Res.* **41** (2008) 2024.
- [10] A.N. Parmar et al., *INTEGRAL mission*, in *X-Ray and Gamma-Ray Telescopes and Instruments for Astronomy*, vol. 4851, pp. 1104–1112, SPIE, 2003.
- [11] L. Bouchet et al., *Diffuse emission measurement with the spectrometer on INTEGRAL as an indirect probe of cosmic-ray electrons and positrons*, *Astrophys. J.* **739** (2011) 29.

- [12] M.D. Mauro et al., *Interpretation of AMS-02 electrons and positrons data*, *JCAP* **2014** (2014) 006.
- [13] O. Adriani et al., *Ten years of PAMELA in space*, *Riv. Nuovo Cim.* **40** (2017) 473.
- [14] O. Adriani et al., *An anomalous positron abundance in cosmic rays with energies 1.5–100 GeV*, *Nature* **458** (2009) 607.
- [15] G. Arcadi et al., *The waning of the WIMP? A review of models, searches, and constraints*, *Eur. Phys. J. C* **78** (2018) 203.
- [16] L. Baudis, *Dark matter searches*, *Ann. Phys. (Berlin)* **528** (2016) 74.
- [17] G. Arcadi et al., *The waning of the WIMP: endgame?*, *Eur. Phys. J. C* **85** (2025) 152.
- [18] P. Cushman et al., *Snowmass CF1 summary: WIMP dark matter direct detection*, *arXiv:1310.8327 [hep-ex]* (2013) .
- [19] J.S. Bullock and M. Boylan-Kolchin, *Small-scale challenges to the Λ CDM paradigm*, *Ann. Rev. Astron. Astrophys.* **55** (2017) 343.
- [20] A.D. Popolo and M.L. Delliou, *Small scale problems of the Λ CDM model: a short review*, *Galaxies* **5** (2017) 17.
- [21] S. Tulin and H.-B. Yu, *Dark matter self-interactions and small scale structure*, *Phys. Rept.* **730** (2018) 1.
- [22] N.Q. Lan, G.J. Mathews, J.A. Coughlin and I.-S. Suh, *Self interacting dark matter and small scale structure*, in *Proceedings of the 15th Marcel Grossmann Meeting on Recent Developments in Theoretical and Experimental General Relativity, Astrophysics, and Relativistic Field Theories*, pp. 1262–1266, World Scientific, 2022.
- [23] S.-M. Choi and H.M. Lee, *Resonant SIMP dark matter*, *Phys. Lett. B* **758** (2016) 47.
- [24] N. Bernal and X. Chu, \mathbb{Z}_2 *SIMP dark matter*, *JCAP* **2016** (2016) 006.
- [25] S. Bhattacharya, P. Ghosh and S. Verma, *SIMPler realisation of scalar dark matter*, *JCAP* **2020** (2020) 040.
- [26] Y. Hochberg et al., *Model for Thermal Relic Dark Matter of Strongly Interacting Massive Particles*, *Phys. Rev. Lett.* (2015) .
- [27] W. Shepherd, T.M.P. Tait and G. Zaharijas, *Bound states of weakly interacting dark matter*, *Phys. Rev. D* (2009) .
- [28] J. March-Russell and S.M. West, *WIMPonium and boost factors for indirect dark matter detection*, *Phys. Lett. B* **676** (2009) 133.
- [29] K. Petraki, M. Postma and M. Wiechers, *Dark-matter bound states from Feynman diagrams*, *JHEP* **06** (2015) 128.
- [30] X. Chu, M. Nikolić and J. Pradler, *Successful Freeze-Out of Strongly Interacting Dark Matter with Even-Numbered Interactions*, *Phys. Rev. Lett.* (2024) .
- [31] J.-X. Pan, M. He, X.-G. He and G. Li, *Scrutinizing a massless dark photon: basis independence*, *Nucl. Phys. B* **953** (2020) 114968.
- [32] J. Buch, M. Cirelli, G. Giesen and M. Taoso, *PPPC 4 DM secondary: a Poor Particle Physicist Cookbook for secondary radiation from Dark Matter*, *JCAP* **2015** (2015) 037.

- [33] M. Cirelli et al., *PPPC 4 DM ID: a poor particle physicist cookbook for dark matter indirect detection*, *JCAP* **2011** (2011) 051.
- [34] S. Girmohanta and R. Shrock, *Cross section calculations in theories of self-interacting dark matter*, *Phys. Rev. D* **106** (2022) 063013.
- [35] W.-Z. Feng, Z.-H. Zhang and K.-Y. Zhang, *Sub-GeV millicharge dark matter from the $U(1)_X$ hidden sector*, *JCAP* **2024** (2024) 112.
- [36] R. Oncala and K. Petraki, *Dark matter bound states via emission of scalar mediators*, *JHEP* **01** (2019) 189.
- [37] A. Messiah, *Quantum Mechanics*, Dover Publications, New York (2014).
- [38] K.Y. Lee, Y.G. Kim and S. Shin, *Singlet fermionic dark matter*, *JHEP* **05** (2008) 100.
- [39] M.D. Mauro et al., *Dark matter in the Higgs resonance region*, *Phys. Rev. D* **108** (2023) 095008.
- [40] T. Binder et al., *Excited bound states and their role in dark matter production*, *Phys. Rev. D* **108** (2023) 095030.
- [41] E. Kolb, *The Early Universe*, CRC Press, Boca Raton (2018).
- [42] J. March-Russell and S.M. West, *WIMPonium and boost factors for indirect dark matter detection*, *Phys. Lett. B* **676** (2009) 133.
- [43] L. Pearce and A. Kusenko, *Indirect detection of self-interacting asymmetric dark matter*, *Phys. Rev. D* **87** (2013) 123531.
- [44] I. Baldes et al., *Indirect searches for dark matter bound state formation and level transitions*, *SciPost Phys.* **9** (2020) 068.
- [45] R. Mahbubani, M. Redi and A. Tesi, *Indirect detection of composite asymmetric dark matter*, *Phys. Rev. D* **101** (2020) 103037.
- [46] K. Petraki, M. Postma and M. Wiechers, *Dark-matter bound states from Feynman diagrams*, *JHEP* **06** (2015) 128.
- [47] H. An, F.P. Huang, J. Liu and W. Xue, *Radio-frequency dark photon dark matter across the sun*, *Phys. Rev. Lett.* **126** (2021) 181102.
- [48] A. Caputo et al., *Dark photon limits: A handbook*, *Phys. Rev. D* **104** (2021) 095029.
- [49] B. von Harling and K. Petraki, *Bound-state formation for thermal relic dark matter and unitarity*, *JCAP* **2014** (2014) 033.
- [50] M. Garny and J. Heisig, *Bound-state effects on dark matter coannihilation: Pushing the boundaries of conversion-driven freeze-out*, *Phys. Rev. D* **105** (2022) 055004.
- [51] M. Cirelli et al., *Integral X-ray constraints on sub-GeV Dark Matter*, *Phys. Rev. D* **103** (2021) 063022.
- [52] T.R. Slatyer, *Indirect detection of dark matter*, in *Anticipating the Next Discoveries in Particle Physics: TASI 2016*, pp. 297–353, World Scientific (2018).
- [53] K.E. O’Donnell and T.R. Slatyer, *Constraints on dark matter with future MeV gamma-ray telescopes*, *Phys. Rev. D* **111** (2025) 083037.
- [54] N.W. Evans, J.L. Sanders and A. Geringer-Sameth, *Simple J-factors and D-factors for indirect dark matter detection*, *Phys. Rev. D* **93** (2016) 103512.

- [55] M. Cirelli et al., *Integral X-ray constraints on sub-GeV Dark Matter*, *Phys. Rev. D* **103** (2021) 063022.
- [56] A. Coogan, L. Morrison and S. Profumo, *Hazma: a python toolkit for studying indirect detection of sub-GeV dark matter*, *JCAP* **2020** (2020) 056.